

Momentum-Space Spin Antivortex and Spin Transport in Monolayer Pb

Kaijie Yang,¹ Yuanxi Wang,^{2,3} and Chao-Xing Liu^{4,*}

¹*Department of Physics, The Pennsylvania State University, University Park, Pennsylvania 16802*

²*2-Dimensional Crystal Consortium, Materials Research Institute,*

The Pennsylvania State University, University Park, Pennsylvania 16802

³*Department of Physics, University of North Texas, Denton, Texas 76203*

⁴*Department of Physics, the Pennsylvania State University, University Park, Pennsylvania 16802*

Nontrivial momentum-space spin texture of electrons can be induced by spin-orbit coupling and underpins various spin transport phenomena, such as current-induced spin polarization and spin Hall effect. In this work, we find that a nontrivial spin texture, spin antivortex, can appear at certain momenta on the $\Gamma - K$ line in 2D monolayer Pb on top of SiC. Different from spin vortex due to the band degeneracy in the Rashba model, the existence of this spin antivortex is guaranteed by the Poincaré-Hopf theorem and thus topologically stable. Accompanied with this spin antivortex, a Lifshitz transition of Fermi surfaces occurs at certain momenta on the $K - M$ line, and both phenomena are originated from the anticrossing between the $j = 1/2$ and $j = 3/2$ bands. A rapid variation of the response coefficients for both the current-induced spin polarization and spin Hall conductivity is found when the Fermi energy is tuned around the spin antivortex. Our work demonstrates monolayer Pb as a potentially appealing platform for spintronic applications.

Introduction – Momentum-space spin textures of electronic bands often provide an intuitive picture to understand spin transport phenomena such as current-induced spin polarization (CISP, also known as the Edelstein effect or the inverse spin galvanic effect)^{1–7} and spin Hall effect (SHE)^{8–10} in spin-orbit coupled materials. The Rashba model^{11–14}, for example, possesses a spin texture of the vortex type, for which electron spins are oriented tangentially along the Fermi contour and form a vortex texture (also called helical texture) for each of the two spin-split bands. Under an electric field, the nonequilibrium distribution of electrons around a shifted Fermi contour carrying spin vortices leads to a net CISP. Such analytical models of spin vortices usually capture spin textures around high-symmetry k points but can be insufficient in describing response functions that rely on *integrals* over the entire Brillouin zone in realistic materials, where complex spin textures arising far from high-symmetry k points contribute dominantly. Here we introduce a new type of spin texture, a *spin antivortex*, with a unique movable but unremovable nature in the momentum space. We demonstrate that spin antivortices can be hosted by atomically thin metals with strong spin orbit coupling (SOC). Such 2D metals have been realized using the confinement heteroepitaxy technique¹⁵, where metal species intercalate underneath graphene epitaxially grown on an insulating SiC substrate. This new growth technique can produce air-stable, crystalline 2D metals at scale, with extraordinary optical¹⁶ and transport properties¹⁵ that may enable the development of new device applications of 2D materials^{17–19}. In particular, the strong SOC in 2D heavy metals, such as Pb, Pt, Sn, Au and Bi, can naturally produce spin-split bands when combined with the inversion symmetry breaking guaranteed by the graphene-metal-SiC architecture.

In this work, we study the spin texture for the 2D Pb monolayer and find that besides the spin vortices around high-symmetry momenta Γ , M and K , spin antivortices

with the opposite winding numbers exist at non-high-symmetry momenta along the $\Gamma - K$ lines, as labelled by six red crosses in Fig. 1(a). Unlike the Rashba model, in which spin vortices are induced by band degeneracy, the spin antivortices in this system are guaranteed by the Poincaré-Hopf theorem, and thus reveal a movable but locally unremovable nature. A Lifshitz transition of the Fermi surface along $K - M$ accompanies the emergence of spin antivortices in a similar energy range. To quantitatively predict the spectroscopic signatures of the spin antivortices and Lifshitz transition, we model their effect on spin transport by combining density functional theory (DFT)^{20–25} with the Green’s function formalism to show that they induce a rapid change of CISP and SHE when the Fermi energy is tuned to align with them. The effect of short-range disorder scattering is also discussed by including the vertex correction in the Green’s function formalism. Our work will guide experimental studies on spin phenomena and pave the way to the spintronic applications of 2D heavy metals.

Lifshitz transition and momentum-space spin antivortex in monolayer Pb – We start from the ground state lattice structure and electronic structure of monolayer Pb on top of SiC substrate. The Pb atoms form a triangular lattice described by the C_{3v} symmetry group that can be generated by a threefold rotation and an in-plane mirror. Inversion symmetry is broken due to the local environment, as shown in Fig. 1(b). The electronic structure of this system at the DFT level (see Supplemental Material⁴⁰ Sec. I.B for details) without and with SOC are, respectively, shown in Fig. 1 (c) and 1(d). Focusing on the -1 to 1 eV energy range near the Fermi energy, the two strongly dispersive bands are mainly characterized by Pb p_x and p_y orbitals; the other weakly dispersive band anticrossing with the p_x and p_y bands is of p_z orbital character from both Pb and the topmost Si layer of the SiC substrate. Band interpolation using maximally localized Wannier functions was then per-

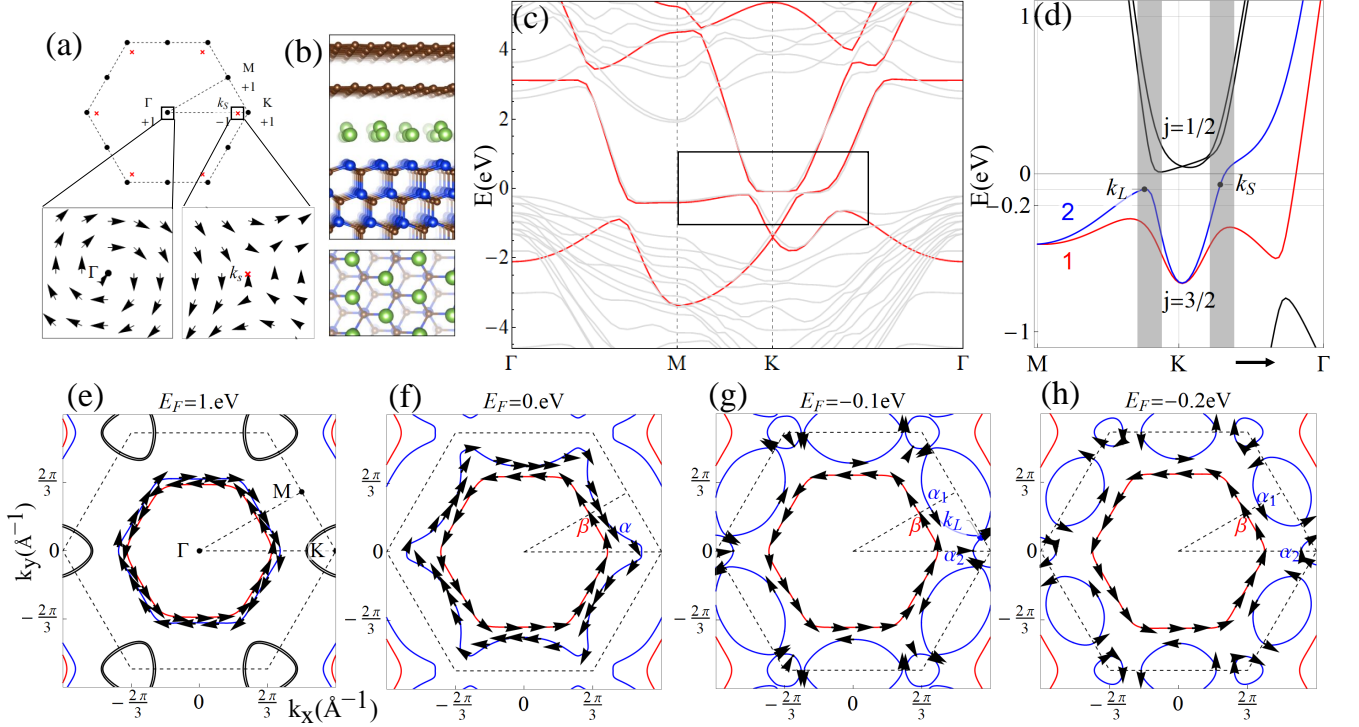


FIG. 1: (a) The locations of spin vortices (black dots) and antivortices (red crosses) in the first BZ and the spin texture for spin vortex around the Γ point with a winding number $+1$ and the antivortex around the k_S point with a winding number -1 . (b) The lattice structure of the intercalated monolayer Pb between SiC substrate and graphene. (c) The electronic band structure without SOC from first principal calculation (gray lines) and from the maximal localized Wannier function (MLWF) (red lines). (d) The band spectrum from MLWF with SOC for the energy range of the black box in (b). The gray region is the anticrossing regime of $j = 1/2$ and $j = 3/2$ bands. k_L and k_S label the locations of the Lifshitz transition point and spin antivortex. (e)–(h) Fermi surfaces and spin texture of band 1 and 2 for $E_F = 1.0, 0.0, -0.1, -0.2$ eV. α (β) are hole pockets for band 1(2) around Γ before the Lifshitz transition. Black lines are electron Fermi pockets. α_1 (α_2) are Fermi surface pockets for band 2 around M (K) after Lifshitz transition.

formed using the above four orbitals for initial projections (details in Supplemental Material⁴⁰). The resulting Wannier-interpolated bands in Fig. 1(c) agrees well with the original DFT ones within the manifold of the four orbitals. After introducing atomic SOC to the tight binding Hamiltonian obtained from Wannierization, we obtain low-energy bands shown in Fig. 1(d). Labeling bands with SOC by total angular momenta j at K , the $j = 1/2$ bands are mainly dominated by Si p_z orbitals and the $j = 3/2$ bands [labeled as bands 1 and 2 in Fig. 1(d)] come from Pb p_x p_y orbitals; these two bands anticross around K for $E_F = -0.1$ eV.

We next show the evolution of Fermi surfaces across a Lifshitz transition in Fig. 1(e-h), where E_F is lowered from 1.0 eV to 0.0, -0.1 and -0.2 eV. At $E_F = 1.0$ eV, the spin-split hole pockets α (blue) and β (red) and the spin-split electron pockets around K (black) come from Pb p_x, p_y orbitals. As the Fermi energy lowers to $E_F = 0.0$ eV, the electron pockets shrink and disappear, while the hole pockets extend towards the Brillouin Zone (BZ) boundary. As the Fermi energy decreases further, the hole pocket α are split into the electron pockets α_1 and

α_2 around the M and K points, as shown in Fig. 1(h). A Lifshitz transition that changes the Fermi surface topology occurs at the momentum k_L along the K – M line at $E_F = -0.1$ eV, as shown in Fig. 1(g).

Also evolving with lowering Fermi energies along Fig. 1(e–h) are spin textures of the Fermi pockets. At $E_F = 1.0$ eV, the spin textures of two hole pockets are of Rashba-type. As the Fermi energy lowers, the spin texture of the inner hole pocket β (red) remains the same while dramatic changes occur for the outer hole pocket α (blue) that experiences the Lifshitz transition. By comparing the spin direction of the blue Fermi pocket at $E_F = 0.0$ and $E_F = -0.2$ eV, one notices that the spin direction of the Fermi pocket α_1 around M at $E_F = -0.2$ eV follows that at $E_F = 0.0$ eV, while the spin direction of the Fermi pocket α_2 around K at $E_F = -0.2$ eV reverses its sign, as compared to that at $E_F = 0.0$ eV. To see this feature more clearly, we focus on the spin texture of band 2 in the whole BZ, as shown in Fig. 2(a), in which the arrows show the in-plane spin directions and the colors indicate the z -component spin. It is clear that the in-plane spin forms vortices around Γ , M , K , and K' .

Zooming in on the spin texture of band 2 around K in Fig. 2(b), we find that, besides the vortex around K, another antivortex centered at k_S appears along the $\Gamma - K$ line. The lines α , α_1 and α_2 in Fig. 2(b) show the Fermi surfaces at $E_F = 0.0$ eV and $E_F = -0.2$ eV, respectively, and we indeed see a sign change of the spin direction for the momenta at the left and right sides of k_S along the $\Gamma - K$ line between these two Fermi surfaces, consistent with the Fermi pocket plot in Fig. 1(f) and 1(h).

The existence of the spin antivortex can be viewed as a consequence of the Poincaré-Hopf theorem of a tangential vector field on a compact manifold²⁶. The BZ is a torus and we only focus on the in-plane spin component, which can be regarded as a tangential field. According to the Poincaré-Hopf theorem, the total of winding numbers around spin vortex is the Euler number of the torus, namely zero. The winding numbers of spin vortices at six high symmetry momenta, namely Γ , K , K' and three M points, are all +1, as shown in Fig. 2(a). On the other hand, there are six antivortices due to the combination of C_3 and \mathcal{T} symmetries, each with winding number -1, as shown in Fig. 1(a). Thus, the total winding number in the whole BZ vanishes, as required by the Poincaré-Hopf theorem. This analysis suggests that, unlike a spin vortex around high symmetry momenta, each spin antivortex is movable along the $\Gamma - K$ lines, but is locally stable due to its topological nature. The difference between spin antivortex and other spin texture, such as spin vortex in the Rashba model, is further discussed in Sec.II.C of Supplemental Material⁴⁰. In addition, it is shown that the location of spin antivortex can be controlled by an external gate voltage, as discussed in Sec.II.B of Supplemental Material⁴⁰.

It is interesting to notice that both the Lifshitz transition and the spin antivortex occur approximately around $E_F \approx -0.1$ eV, as shown in Fig. 2(b). This is because both phenomena are related to the anticrossings between the $j = 1/2$ bands from p_z orbitals and the $j = 3/2$ bands from $p_{x,y}$ orbitals around K or K' , as shown by the gray regime in Fig. 1(d). We provide more detailed analysis on how the band anticrossing can induce the Lifshitz transition and spin antivortex in Supplemental Material⁴⁰ Sec.II.B.

Current-induced spin polarization and spin Hall effect

– The Lifshitz transition and spin antivortex can be experimentally verified by their spectroscopic signatures: they can, in principle, be extracted through the spin-resolved angular-resolved photoemission spectroscopy²⁷. Here we focus on the spin transport phenomena of CISP and SHE, which are described by the response equations, $S_k = \sum_i \chi_{ki} E_i$ for CISP and $J_j^k = \sum_i \sigma_{ji}^k E_i$ for SHE, respectively. Here S_k is the spin operator with $k = x, y, z$, v_j is the velocity operator with $i, j = x, y$ and $J_j^k = \{S_k, v_j\}/2$ is the spin current operator. Based on the threefold rotation and in-plane mirror symmetries, the nonzero in-plane current response coefficients for x -direction electrical field are χ_{yx} for CISP and $\sigma_{yx}^z, \sigma_{xx}^x = -\sigma_{yx}^y$ for SHE from the Neumann's principles²⁸.

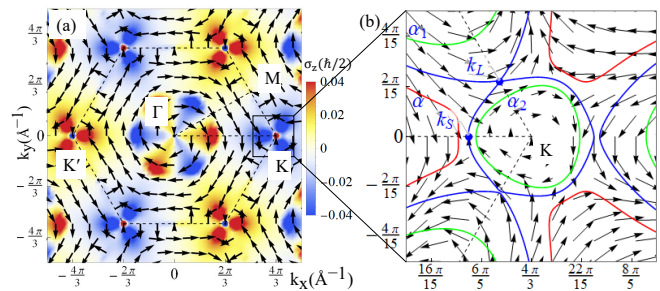


FIG. 2: (a) Spin texture of the band 2 in the whole BZ. The arrows depict in-plane spin polarization while the background color reveals the z -component spin polarization. The spin vortices with winding number +1 exist at high symmetry points Γ , M , K , K' . (b) The zoom-in of spin texture around K . A spin antivortex shows up on the $\Gamma - K$ line at k_S point on Fermi surfaces around $E_F = -0.1$ eV, concurrent with the Lifshitz transition. The red, blue, green lines are Fermi surfaces of $E_F = 0.0, -0.1, -0.2$ eV respectively.

The detailed form of the response coefficients χ_{ij} and σ_{ji}^k can be derived from the standard linear response theory and are given by

$$\begin{aligned} \chi_{ij}(E_F) &= \int \frac{d^2 \mathbf{k}}{(2\pi)^2} \chi_{ij}(\mathbf{k}, E_F) \\ &= -\frac{1}{2\pi} \int \frac{d^2 \mathbf{k}}{(2\pi)^2} \text{Tr} S_i G^R(\mathbf{k}, E_F) \Gamma_j(\mathbf{k}) G^A(\mathbf{k}, E_F) \end{aligned} \quad (1)$$

and

$$\begin{aligned} \sigma_{ij}^k(E_F) &= \int \frac{d^2 \mathbf{k}}{(2\pi)^2} \sigma_{ij}^k(\mathbf{k}, E_F) \\ &= -\frac{1}{2\pi} \int \frac{d^2 \mathbf{k}}{(2\pi)^2} \text{Tr} J_i^k(\mathbf{k}) G^R(\mathbf{k}, E_F) \Gamma_j(\mathbf{k}) G^A(\mathbf{k}, E_F) \end{aligned} \quad (2)$$

where G^R and G^A are the retarded and advanced Green's functions, Tr is the trace taken over band indices, and the vertex operator $\Gamma_j(\mathbf{k})$ is defined as $\Gamma_j(\mathbf{k}, E) = J_j(\mathbf{k}) + \gamma_j(E)$ with the current operator $J_j = -ev_j$ and

$$\gamma_j(E) = n_i V_0^2 \int \frac{d^2 \mathbf{l}}{(2\pi)^2} G^R(\mathbf{l}, E) (J_j(\mathbf{l}, E) + \gamma_j(E)) G^A(\mathbf{l}, E). \quad (3)$$

Here, γ_j describes the vertex correction to the current operator from the ladder diagram of disorder scattering with the disorder density n_i and scattering strength V_0 ²⁹. We apply the linear response formalism to the above-mentioned tight-binding model parametrized using Wannier functions; details of the numerical technique are discussed in Supplemental Material⁴⁰ Sec. I.

Fig. 3 summarizes our main numerical results for $\chi_{yx}(E_F)$ for CISP and $\sigma_{yx}^z(E_F)$ for SHE, respectively. Here the green line is for the case without the vertex correction, namely $\Gamma_j(\mathbf{k}, E) = J_j(\mathbf{k})$, and the black line with vertex correction. We first analyze $\chi_{yx}(E_F)$ and plot its momentum resolved contribution $\chi_{yx}(\mathbf{k}, E_F)$ of

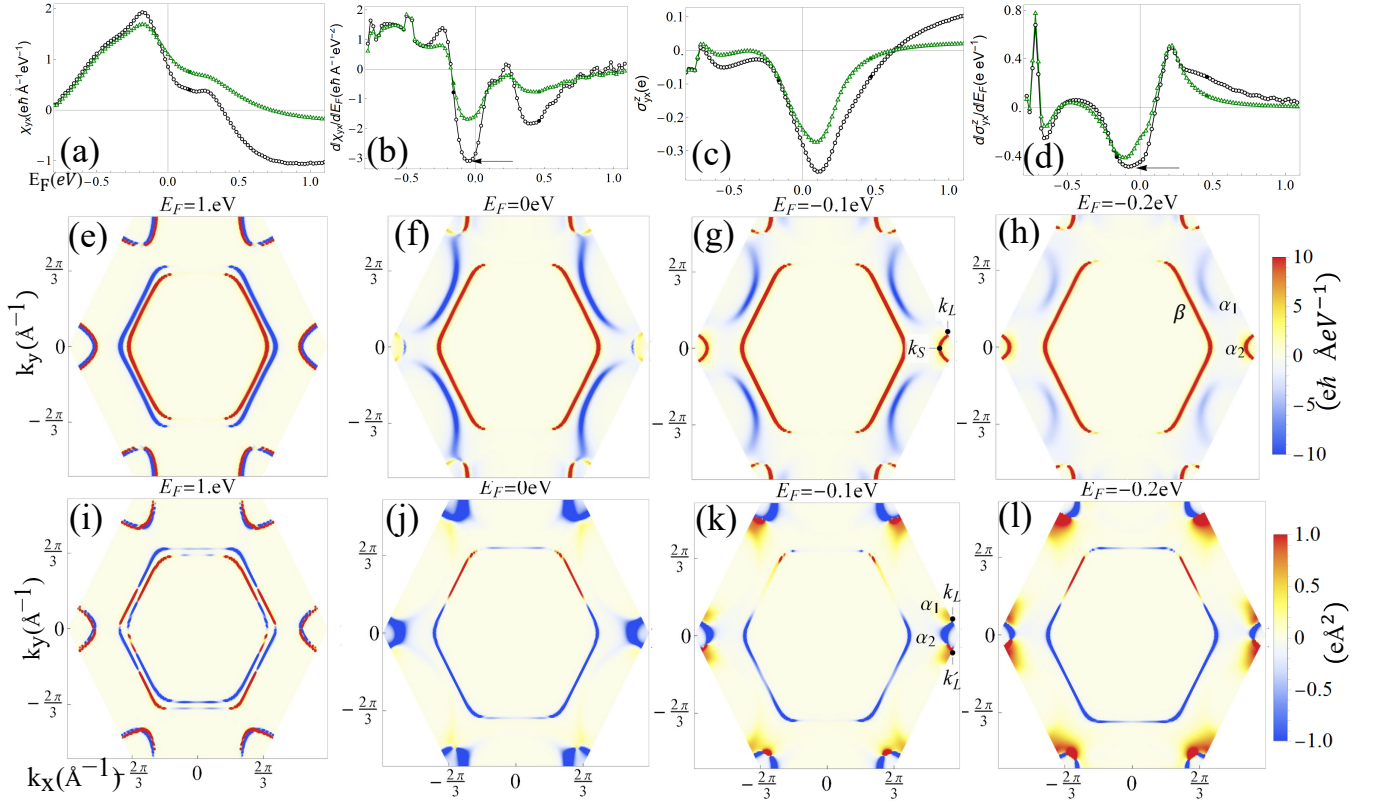


FIG. 3: (a), (b), (c) and (d) show χ_{yx} , $d\chi_{yx}/dE_F$, σ_{yx}^z , and $d\sigma_{yx}^z/dE_F$, respectively, as a function of E_F , in the clean case (black lines with circles) and with disorder scattering (green lines with triangles) for different E_F . (e)–(h) and (i)–(l) show the momentum resolved contribution $\chi_{ij}(\mathbf{k}, E_F)$ to the CISP and $\sigma_{ij}^k(\mathbf{k}, E_F)$ to the SHE, respectively, over the BZ for $E_F = 1.0, 0.0, -0.1, -0.2$ eV (without vertex correction).

Eq. (1) in Fig. 3(e)–3(i). We find that the main contribution to CISP comes from the Fermi surface since $G^R(\mathbf{k}, E_F)G^A(\mathbf{k}, E_F)$ in (1) can be approximated by $\delta(E_F - \epsilon_{nk})$ in the dilute disorder limit. At $E_F = 1.0$ eV, due to the opposite spin texture for the two hole pockets, they contribute oppositely to CISP, as shown in Fig. 3(e). The outer Fermi pocket will be dominant and thus gives rise to the negative sign of γ_{yx} , resembling the CISP contribution in the standard Rashba model¹¹. Near the Lifshitz transition, a dramatic change occurs to the outer Fermi pocket α_2 around K and K' . When lowering the Fermi energy from $E_F = 0.0$ to -1.0 eV, one can clearly see that the Fermi pocket α_2 around K and K' varies from blue (negative) to red (positive), as shown in Fig. 3(f) and 3(g). Physically, this sign change directly reflects the presence of spin antivortices, as the spin direction on the Fermi pocket α_2 around K and K' changes its sign across the spin antivortex. In addition, the contribution to CISP from the Fermi pocket α_1 around M also decreases due to the reduction of relaxation time (See Sec. II.C of Supplemental Material⁴⁰). Combining the above factors leads to (i) the positive sign of χ_{yx} in this Fermi energy range ($E_F < 0.3$ eV) and (ii) a rapid increase of χ_{yx} around $E_F \approx -0.1$ eV as E_F decreases. To see this rapid change more clearly, we

take a derivative of χ_{yx} with respect to E_F , as shown in Fig. 3(b). The peak in the amplitude of $d\chi_{yx}/dE_F$ indeed occurs around $E_F \approx -0.1$ eV, as shown by the arrow in Fig. 3(b), and thus is induced by the Fermi surface crossing the antivortex. The SHE also reveals a rapid change around $E_F \approx -0.1$ eV, as shown by a similar peak appears for $d\sigma_{yx}^z/dE_F$ in Fig. 3(d). This is because the contribution to SHE around the Fermi pockets α_1 close to the Lifshitz transition point k_L and that around α_2 close to k'_L abruptly changes sign from negative (blue) to positive (red) when lowering the Fermi energy from $E_F = 0.0$ to -0.1 eV, as shown in Fig. 3(j) and 3(k). Detailed analysis suggests that the sign change of contribution around k_L and k'_L is more closely related to the Lifshitz transition due to the fact that the SHE mainly is contributed from interband matrix elements rather than the intraband Fermi surface contribution, as discussed in Sec. II.D of Supplemental Material⁴⁰. The influence of disorder scattering is also evaluated through the vertex correction, as shown by the dashed lines in Fig. 3(a), 3(b) and 3(c), 3(d). We generally find both the values of χ_{yx} and σ_{yx}^z , as well as $d\chi_{yx}/dE_F$ and $d\sigma_{yx}^z/dE_F$, around $E_F = 1.0$ eV are enhanced by disorder scattering, as discussed in details in Sec. II.C and II.D of Supplemental Material⁴⁰.

Conclusion and discussion – In conclusion, the spin antivortices and Lifshitz transition induced by the anticrossing between the p_z and $p_{x,y}$ bands strongly affect spin transport phenomena in the monolayer Pb on SiC. By choosing appropriate parameters (see Sec.II.E of Supplemental Material⁴⁰), we find σ_{yx}^z is of the order $10^{-1}e$ in our model and the corresponding spin Hall angle is $\sim 10^{-2}$, comparable to the existing experimentally measured values^{30–32}. Based on the same values, we find the variation of σ_{yx}^z across the band anticrossing regime is around $\sim 0.3e$, and thus should be measurable by tuning the carrier density of 2D Pb in experiments. For CISP, χ_{yx}/\hbar is of the order $10^{-8} \text{ nm}^{-2}\text{V}^{-1}\text{m}$ and its variation is $\sim 2 \times 10^{-8} \text{ nm}^{-2}\text{V}^{-1}\text{m}$ in the band anticrossing regime. The charge-to-spin conversion efficiency $2ev_f\chi_{yx}/\hbar\sigma_{xx}$ is

~ 0.1 , where v_f is the Fermi velocity and σ_{xx} is the longitudinal conductivity. This efficiency is close to that proposed and measured of graphene on a transition-metal dichalcogenide^{33,34}. While Pb films have been grown on top of SiC with different growth methods^{35–39}, our theory suggests the monolayer Pb as an excellent platform for the study of spin transport phenomena and spintronic applications.

Acknowledgments– We thank V. Crespi, J. Robinson, N. Samarth, W. Yanez and J. Zhu for helpful discussions. This work is mainly supported by the Penn State MRSECCenter for Nanoscale Science via NSF Grant No. DMR-2011839. C.-X. L. also acknowledges the support of the Office of Naval Research (Grant No. N00014-18-1-2793).

-
- * Electronic address: cxl56@psu.edu
- ¹ V. M. Edelstein, Solid State Communications **73**, 233 (1990).
 - ² Y. Kato, R. Myers, A. Gossard, and D. Awschalom, Physical Review Letters **93**, 176601 (2004).
 - ³ A. Y. Silov, P. Blajnov, J. Wolter, R. Hey, K. Ploog, and N. Averkiev, Applied physics letters **85**, 5929 (2004).
 - ⁴ V. Sih, R. Myers, Y. Kato, W. Lau, A. Gossard, and D. Awschalom, Nature Physics **1**, 31 (2005).
 - ⁵ H. Zhang, S. Yamamoto, B. Gu, H. Li, M. Maekawa, Y. Fukaya, and A. Kawasuso, Physical review letters **114**, 166602 (2015).
 - ⁶ C. H. Li, O. M. van't Erve, S. Rajput, L. Li, and B. T. Jonker, Nature communications **7**, 1 (2016).
 - ⁷ I. Žutić, J. Fabian, and S. D. Sarma, Reviews of modern physics **76**, 323 (2004).
 - ⁸ J. Hirsch, Physical review letters **83**, 1834 (1999).
 - ⁹ J. Sinova, D. Culcer, Q. Niu, N. Sinitsyn, T. Jungwirth, and A. H. MacDonald, Physical review letters **92**, 126603 (2004).
 - ¹⁰ S. Murakami, N. Nagaosa, and S.-C. Zhang, Science **301**, 1348 (2003).
 - ¹¹ J.-i. Inoue, G. E. Bauer, and L. W. Molenkamp, Physical Review B **67**, 033104 (2003).
 - ¹² M. Trushin and J. Schliemann, Physical Review B **75**, 155323 (2007).
 - ¹³ A. Johansson, J. Henk, and I. Mertig, Physical Review B **93**, 195440 (2016).
 - ¹⁴ J.-i. Inoue, G. E. Bauer, and L. W. Molenkamp, Physical Review B **70**, 041303 (2004).
 - ¹⁵ N. Briggs, B. Bersch, Y. Wang, J. Jiang, R. J. Koch, N. Nayir, K. Wang, M. Kolmer, W. Ko, A. D. L. F. Duran, et al., Nature materials **19**, 637 (2020).
 - ¹⁶ M. A. Steves, Y. Wang, N. Briggs, T. Zhao, H. El-Sherif, B. M. Bersch, S. Subramanian, C. Dong, T. Bowen, A. D. L. Fuente Duran, et al., Nano letters **20**, 8312 (2020).
 - ¹⁷ P. Miró, M. Audiffred, and T. Heine, Chemical Society Reviews **43**, 6537 (2014).
 - ¹⁸ A. Avsar, H. Ochoa, F. Guinea, B. Özyilmaz, B. Van Wees, and I. J. Vera-Marun, Reviews of Modern Physics **92**, 021003 (2020).
 - ¹⁹ S. Das, J. A. Robinson, M. Dubey, H. Terrones, and M. Terrones, Annual Review of Materials Research **45**, 1 (2015).
 - ²⁰ G. Guo, Y. Yao, and Q. Niu, Physical review letters **94**, 226601 (2005).
 - ²¹ G.-Y. Guo, S. Murakami, T.-W. Chen, and N. Nagaosa, Physical review letters **100**, 096401 (2008).
 - ²² F. Freimuth, S. Blügel, and Y. Mokrousov, Physical review letters **105**, 246602 (2010).
 - ²³ S. Lowitzer, M. Gradhand, D. Ködderitzsch, D. V. Fedorov, I. Mertig, and H. Ebert, Physical review letters **106**, 056601 (2011).
 - ²⁴ M. Gradhand, D. V. Fedorov, P. Zahn, and I. Mertig, Physical review letters **104**, 186403 (2010).
 - ²⁵ M. Gradhand, D. V. Fedorov, P. Zahn, and I. Mertig, Physical Review B **81**, 245109 (2010).
 - ²⁶ W. Fulton, *Algebraic topology: a first course*, vol. 153 (Springer Science & Business Media, 2013).
 - ²⁷ J. A. Sobota, Y. He, and Z.-X. Shen, Reviews of Modern Physics **93**, 025006 (2021).
 - ²⁸ F. E. Neumann and O. E. Meyer, *Vorlesungen über die Theorie der Elasticität der festen Körper und des Lichtäthers, gehalten an der Universität Königsberg* (B.G. Teubner, 1885).
 - ²⁹ G. D. Mahan, *Many-particle physics* (Springer Science & Business Media, 2013).
 - ³⁰ M. Morota, Y. Niimi, K. Ohnishi, D. Wei, T. Tanaka, H. Kontani, T. Kimura, and Y. Otani, Physical Review B **83**, 174405 (2011).
 - ³¹ O. Mosendz, V. Vlaminc, J. Pearson, F. Fradin, G. Bauer, S. Bader, and A. Hoffmann, Physical Review B **82**, 214403 (2010).
 - ³² K. Ando and E. Saitoh, Journal of Applied Physics **108**, 113925 (2010).
 - ³³ T. S. Ghiasi, A. A. Kaverzin, P. J. Blah, and B. J. van Wees, Nano letters **19**, 5959 (2019).
 - ³⁴ M. Offidani, M. Milletari, R. Raimondi, and A. Ferreira, Physical review letters **119**, 196801 (2017).
 - ³⁵ A. Yurtsever, J. Onoda, T. Iimori, K. Niki, T. Miyamachi, M. Abe, S. Mizuno, S. Tanaka, F. Komori, and Y. Sugimoto, Small **12**, 3956 (2016).
 - ³⁶ S. Chen, P. A. Thiel, E. Conrad, and M. C. Tringides, Physical Review Materials **4**, 124005 (2020).
 - ³⁷ J. Wang, M. Kim, L. Chen, K.-M. Ho, M. Tringides, C.-Z. Wang, and S. Wang, Physical Review B **103**, 085403 (2021).

- (2021).
- ³⁸ M. Hupalo, X. Liu, C.-Z. Wang, W.-C. Lu, Y.-X. Yao, K.-M. Ho, and M. C. Tringides, *Advanced Materials* **23**, 2082 (2011).
- ³⁹ X. Liu, T. Hu, Y. Miao, D. Ma, P. K. Chu, F. Ma, and K. Xu, *Journal of Applied Physics* **117**, 065304 (2015).
- ⁴⁰ See Supplemental Material for construction of the tight binding model from DFT and detailed numerical calculation of spin transport response functions for Rashba 2DEG and 2D Pb, which includes Refs. [41-53].
- ⁴¹ J. P. Perdew, K. Burke, and M. Ernzerhof, *Phys. Rev. Lett.* **77**, 3865 (1996).
- ⁴² J. P. Perdew, K. Burke, and M. Ernzerhof, *Phys. Rev. Lett.* **78**, 1396 (1997).
- ⁴³ P. E. Blöchl, *Phys. Rev. B* **50**, 17953 (1994).
- ⁴⁴ G. Kresse and D. Joubert, *Phys. Rev. B* **59**, 1758 (1999), 0927-0256(96)00008.
- ⁴⁵ G. Kresse and J. Furthmüller, *Phys. Rev. B* **54**, 11169 (1996).
- ⁴⁶ S. Grimme, J. Antony, S. Ehrlich, and H. Krieg, *J. Chem. Phys.* **132**, 154104 (2010).
- ⁴⁷ P. Giannozzi, S. Baroni, N. Bonini, M. Calandra, R. Car, C. Cavazzoni, D. Ceresoli, G. L. Chiarotti, M. Cococcioni, I. Dabo, et al., *J. Phys. Condens. Matter* **21**, 395502 (2009), 0906.2569.
- ⁴⁸ N. Marzari and D. Vanderbilt, *Phys. Rev. B* **56**, 12847 (1997).
- ⁴⁹ A. A. Mostofi, J. R. Yates, Y.-S. Lee, I. Souza, D. Vanderbilt, and N. Marzari, *Comput. Phys. Commun.* **178**, 685 (2008).
- ⁵⁰ I. Souza, N. Marzari, and D. Vanderbilt, *Phys. Rev. B* **65**, 035109 (2001).
- ⁵¹ Y.-W. Wei, C.-K. Li, Y. Cao, and J. Feng, *Computer Physics Communications* **258**, 107551 (2021).
- ⁵² J. C. A. Barata and M. S. Hussein, *Brazilian Journal of Physics* **42**, 146 (2012).
- ⁵³ J. Sinova, S. O. Valenzuela, J. Wunderlich, C. Back, and T. Jungwirth, *Reviews of Modern Physics* **87**, 1213 (2015).

Supplementary Materials of "Momentum-space Spin Anti-vortex and Spin Transport in Monolayer Pb"

Kaijie Yang,¹ Yuanxi Wang,^{2,3} and Chao-Xing Liu^{1,*}

¹*Department of Physics, the Pennsylvania State University, University Park, PA 16802*

²*2-Dimensional Crystal Consortium, Materials Research Institute,*

The Pennsylvania State University, University Park, PA 16802

³*Department of Physics, University of North Texas, Denton, TX 76203*

I. NUMERICAL LINEAR RESPONSE OF SPIN TRANSPORT WITH SHORT RANGE DISORDER

A. formalism

The formalism for CISP χ_{ij} and SHE σ_{ij}^k in orbital basis are derived from the linear response theory¹ and are given in the main text by

$$\chi_{ij} = -\frac{1}{2\pi} \int \frac{d^2\mathbf{k}}{(2\pi)^2} \text{Tr} S_i G^R(\mathbf{k}, E_f) \Gamma_j(\mathbf{k}, E_f) G^A(\mathbf{k}, E_f) \quad (1)$$

and

$$\sigma_{ij}^k = -\frac{1}{2\pi} \int \frac{d^2\mathbf{k}}{(2\pi)^2} \text{Tr} J_i^k(\mathbf{k}) G^R(\mathbf{k}, E_f) \Gamma_j(\mathbf{k}, E_f) G^A(\mathbf{k}, E_f) \quad (2)$$

where the Green's functions are defined as

$$G^R(\mathbf{k}, E) = (E - H(\mathbf{k}) - \Sigma^R(E))^{-1}. \quad (3)$$

The integrand

$$\chi_{ij}(\mathbf{k}) = -\frac{1}{2\pi} \text{Tr} S_i G^R(\mathbf{k}, E_f) \Gamma_j(\mathbf{k}, E_f) G^A(\mathbf{k}, E_f) \quad (4)$$

is defined as the contribution over the Brillouin zone (BZ) to CISP. The contribution over BZ to SHE is also defined similarly for the integrand

$$\sigma_{ij}^k(\mathbf{k}) = -\frac{1}{2\pi} \text{Tr} J_i^k(\mathbf{k}) G^R(\mathbf{k}, E_f) \Gamma_j(\mathbf{k}, E_f) G^A(\mathbf{k}, E_f). \quad (5)$$

The self energies $\Sigma^R(\mathbf{k}, E)$ in the Green's functions come from short range disorder. The disorder has the δ -like potential $V(\mathbf{r}) = \sum_i V_0 \delta(\mathbf{r} - \mathbf{R}_i)$ and the density n_i where V_0 is the disorder strength and R_i is the disorder position. After disorder average, the self energies in the self-consistent Born approximation are

$$\Sigma^R(E) = n_i V_0^2 \int \frac{d^2\mathbf{k}'}{(2\pi)^2} G^R(\mathbf{k}', E). \quad (6)$$

The vertex correction $\Gamma_j(\mathbf{k}, E) = J_j(\mathbf{k}) + \gamma_j(E)$ is written in the ladder approximation as in the main text

$$\gamma_j(E) = n_i V_0^2 \int \frac{d^2\mathbf{l}}{(2\pi)^2} G^R(\mathbf{l}, E) (J_j(\mathbf{l}) + \gamma_j(E)) G^A(\mathbf{l}, E). \quad (7)$$

The $\gamma_j(E)$ is independent of momenta because the δ -like disorder potential $V(\mathbf{r})$ becomes a constant $V(\mathbf{k} - \mathbf{l})$ for all transferred momenta after the transform to the momentum space.

When the disorder is dilute, the formalism transformed to energy eigenspace of Hamiltonian can be reduced to the Fermi surfaces. The self-consistent Born approximation for self energies is reduced to first-order Born approximation and reads

$$\text{Im} \Sigma^R(\mathbf{k}n, E) = n_i V_0^2 \sum_{n'} \int \frac{d^2\mathbf{k}'}{(2\pi)^2} (-\pi) \delta(E - \epsilon_{\mathbf{k}'n'}) |\langle \mathbf{k}n | \mathbf{k}'n' \rangle|^2. \quad (8)$$

The $|\mathbf{k}n\rangle$ are the eigen states of Hamiltonian and $\epsilon_{\mathbf{k}n}$ are the corresponding eigen energies. The imaginary part of the bare Green's function in energy eigenspace $G_0^R(\mathbf{k}n, E) = (E - \epsilon_{\mathbf{k}n} + i0^+)^{-1}$ is approximated by $-\pi\delta(E - \epsilon_{\mathbf{k}n})$. The δ -function shows the contribution to self-energies come from the Fermi surface. The off-diagonal parts of self energies in eigen-energy space are dropped. Under the time reversal symmetry \mathcal{T} , the diagonal self-energies become

$$\begin{aligned}\text{Im}\Sigma^R(\mathbf{k}n, E) &= n_i V_0^2 \sum_{n'} \int \frac{d^2\mathbf{k}'}{(2\pi)^2} (-\pi)\delta(E - \epsilon_{\mathbf{k}'n'}) |\langle \mathbf{k}n | \mathcal{T}^\dagger \mathcal{T} | \mathbf{k}'n' \rangle|^2. \\ &= n_i V_0^2 \sum_{n'} \int \frac{d^2\mathbf{k}'}{(2\pi)^2} (-\pi)\delta(E - \epsilon_{\mathbf{k}'n'}) | \langle -\mathbf{k}'n | -\mathbf{k}n' \rangle|^2 \\ &= \text{Im}\Sigma^R(-\mathbf{k}n, E).\end{aligned}\quad (9)$$

The relaxation time is

$$\tau_{\mathbf{k}n}(E) = \frac{-1}{2 \text{Im}\Sigma^R(\mathbf{k}n, E)}.\quad (10)$$

To evaluate the CISP in Eq. (1), we consider the approximation

$$G^R(\mathbf{k}n, E)G^A(\mathbf{k}n', E) \approx \delta_{nn'}\delta(E - \epsilon_{\mathbf{k}n}) \frac{\pi}{-\text{Im}\Sigma^R(\mathbf{k}n, E)},\quad (11)$$

in which the off-diagonal part $n \neq n'$ is of the order $\text{Im}\Sigma^R/(\epsilon_{\mathbf{k}n} - \epsilon_{\mathbf{k}n'})$, as compared to diagonal part $n = n'$, and thus is neglected. Under this approximation, the response coefficient χ_{ij} of the CISP in energy eigenspace reads

$$\chi_{ij} = -\frac{1}{2\pi} \sum_n \int \frac{d^2\mathbf{k}}{(2\pi)^2} \langle \mathbf{k}n | S_i | \mathbf{k}n \rangle \langle \mathbf{k}n | \Gamma_j(\mathbf{k}, E_f) | \mathbf{k}n \rangle \delta(E_f - \epsilon_{\mathbf{k}n}) \frac{\pi}{-\text{Im}\Sigma^R(\mathbf{k}n, E_f)}.\quad (12)$$

Below we will also consider the integrand

$$\chi_{ij}(\mathbf{k}) = -\frac{1}{2\pi} \langle \mathbf{k}n | S_i | \mathbf{k}n \rangle \langle \mathbf{k}n | \Gamma_j(\mathbf{k}, E_f) | \mathbf{k}n \rangle \delta(E_f - \epsilon_{\mathbf{k}n}) \frac{\pi}{-\text{Im}\Sigma^R(\mathbf{k}n, E_f)},\quad (13)$$

which reveals the momentum-resolved contribution around the Fermi surfaces of the band n . Under the similar approximation, the vertex correction reads

$$\gamma_j(\mathbf{k}n, E) = n_i V_0^2 \sum_m \int \frac{d^2\mathbf{l}}{(2\pi)^2} (J_j(\mathbf{l}m) + \gamma_j(\mathbf{l}m, E)) |\langle \mathbf{k}n | \mathbf{l}m \rangle|^2 \delta(E - \epsilon_{\mathbf{l}m}) \frac{\pi}{-\text{Im}\Sigma^R(\mathbf{l}m, E)}\quad (14)$$

where $\gamma_j(\mathbf{k}n, E) = \langle \mathbf{k}n | \gamma_j(E) | \mathbf{k}n \rangle$ and $J_j(\mathbf{k}n) = \langle \mathbf{k}n | J_j(\mathbf{k}) | \mathbf{k}n \rangle$. After obtaining $\gamma_j(\mathbf{k}n, E)$, the off-diagonal part of the vertex correction is

$$\langle \mathbf{k}n | \gamma_j(E) | \mathbf{k}n' \rangle = n_i V_0^2 \sum_m \int \frac{d^2\mathbf{l}}{(2\pi)^2} (J_j(\mathbf{l}m) + \gamma_j(\mathbf{l}m, E)) \langle \mathbf{k}n | \mathbf{l}m \rangle \langle \mathbf{l}m | \mathbf{k}n' \rangle \delta(E - \epsilon_{\mathbf{l}m}) \frac{\pi}{-\text{Im}\Sigma^R(\mathbf{l}m, E)}.\quad (15)$$

The vertex correction can also be calculated for the spin operator in CISP as

$$\langle \mathbf{k}n | \gamma_i^S(E) | \mathbf{k}n \rangle = n_i V_0^2 \sum_m \int \frac{d^2\mathbf{l}}{(2\pi)^2} (\langle \mathbf{l}m | S_i | \mathbf{l}m \rangle + \langle \mathbf{l}m | \gamma_i^S(E) | \mathbf{l}m \rangle) |\langle \mathbf{k}n | \mathbf{l}m \rangle|^2 \delta(E - \epsilon_{\mathbf{l}m}) \frac{\pi}{-\text{Im}\Sigma^R(\mathbf{l}m, E)}.\quad (16)$$

The spin operator with the vertex correction is

$$\langle \mathbf{k}n | \tilde{S}_i(E) | \mathbf{k}n \rangle = \langle \mathbf{k}n | S_i + \gamma_i^S(E) | \mathbf{k}n \rangle.\quad (17)$$

For SHE, Eq. (2) is divided into diagonal parts and off diagonal parts in energy eigenspace as

$$\sigma_{ij}^k = \sigma^D + \sigma^{OD}.\quad (18)$$

The diagonal (intraband) contribution is

$$\sigma^D = -\frac{1}{2\pi} \sum_n \int \frac{d^2\mathbf{k}}{(2\pi)^2} \langle \mathbf{k}n | J_i^k | \mathbf{k}n \rangle \langle \mathbf{k}n | \Gamma_j | \mathbf{k}n \rangle \delta(E_f - \epsilon_{\mathbf{k}n}) \frac{\pi}{-\text{Im}\Sigma^R(\mathbf{k}n, E_f)}.\quad (19)$$

Under \mathcal{T} , the diagonal part becomes

$$\begin{aligned}\sigma^D &= -\frac{1}{2\pi} \sum_n \int \frac{d^2\mathbf{k}}{(2\pi)^2} \langle -\mathbf{k}n | (\mathcal{T} J_i^k \mathcal{T}^\dagger) | -\mathbf{k}n \rangle^* \langle -\mathbf{k}n | (\mathcal{T} \Gamma_j \mathcal{T}^\dagger) | -\mathbf{k}n \rangle^* \delta(E_f - \epsilon_{\mathbf{k}n}) \frac{\pi}{-\text{Im} \Sigma^R(\mathbf{k}n, E_f)} \\ &= -\frac{1}{2\pi} \sum_n \int \frac{d^2\mathbf{k}}{(2\pi)^2} \langle \mathbf{k}n | (J_i^k) | \mathbf{k}n \rangle \langle \mathbf{k}n | (-\Gamma_j) | \mathbf{k}n \rangle \delta(E_f - \epsilon_{-\mathbf{k}n}) \frac{\pi}{-\text{Im} \Sigma^R(-\mathbf{k}n, E_f)} \\ &= -\sigma^D.\end{aligned}\tag{20}$$

So the intraband contribution to SHE is zero. The off diagonal part of the real SHE conductivity reads

$$\sigma_{ij}^k = \sigma^{OD} = -\frac{1}{2\pi} \sum_{n \neq n'} \int \frac{d^2\mathbf{k}}{(2\pi)^2} (-) \text{Im}(G^R(\mathbf{k}n, E_f) G^A(\mathbf{k}n', E_f)) \text{Im}(\langle \mathbf{k}n' | J_i^k | \mathbf{k}n \rangle \langle \mathbf{k}n | \Gamma_j(\mathbf{k}, E_f) | \mathbf{k}n' \rangle)\tag{21}$$

where the term $\text{Re}(G^R(\mathbf{k}n, E) G^A(\mathbf{k}n', E))$ is neglected because it is of the order $\text{Im}(\Sigma^R)^2/(\epsilon_{\mathbf{k}n} - \epsilon_{\mathbf{k}n'})^2$ compared to the $\text{Im}(G^R(\mathbf{k}n, E) G^A(\mathbf{k}n', E))$. Adopting the approximation

$$\text{Im}(G^R(\mathbf{k}n, E) G^A(\mathbf{k}n', E)) \approx (-\pi)(\delta(E - \epsilon_{\mathbf{k}n}) + \delta(E - \epsilon_{\mathbf{k}n'})) \frac{1}{\epsilon_{\mathbf{k}n} - \epsilon_{\mathbf{k}n'}},\tag{22}$$

we find the SHE from the Fermi surface contribution is

$$\sigma_{ij}^k = -\frac{1}{2\pi} \sum_{n \neq n'} \int \frac{d^2\mathbf{k}}{(2\pi)^2} 2\pi \delta(E_f - \epsilon_{\mathbf{k}n}) \frac{1}{\epsilon_{\mathbf{k}n} - \epsilon_{\mathbf{k}n'}} \text{Im}(\langle \mathbf{k}n' | J_i^k | \mathbf{k}n \rangle \langle \mathbf{k}n | \Gamma_j(\mathbf{k}, E_f) | \mathbf{k}n' \rangle).\tag{23}$$

We also define the momentum-resolved contribution to the SHE as

$$\sigma_{ij}^k(\mathbf{k}n) = -\frac{1}{2\pi} \sum_{n'} 2\pi \delta(E_f - \epsilon_{\mathbf{k}n}) \frac{1}{\epsilon_{\mathbf{k}n} - \epsilon_{\mathbf{k}n'}} \text{Im}(\langle \mathbf{k}n' | J_i^k | \mathbf{k}n \rangle \langle \mathbf{k}n | \Gamma_j(\mathbf{k}, E_f) | \mathbf{k}n' \rangle)\tag{24}$$

at the Fermi surface of the band n .

In our numerical simulations, we directly evaluate Eq. (1) and Eq. (2) over the first Brillouin zone. The numerical results can be well understood from the simplified expressions of Eq. (12) and Eq. (23), which only depends on the contribution from the Fermi energy.

B. Constructing the Tight Binding Model from DFT

Density functional theory (DFT) calculations were based on the relaxed structure of monolayer Pb on SiC, where Pb coverage is 100%, i.e. one Pb per surface Si atom. We focus on this surface phase here since it is the thermodynamic ground state in a wide range of Pb chemical potentials compared with competing surface phases where Pb coverage is partial. Within candidate structures satisfying 100% coverage, the registry where each Pb is directly on top of a surface Si site is preferred against the two other high-symmetry registries (Pb projecting onto the topmost C site or a ‘‘hollow’’ site, as defined in Ref. [2]). The relaxed Pb structure features one out of every three Pb atom buckling out-of-plane. C_{3v} symmetry is preserved even when this buckling is considered, since our supercell was chosen to be minimal and includes just three Pb atoms.

For DFT-level structural relaxations, the Perdew-Burke-Ernzerhof (PBE) parametrization of the exchange-correlation functional at the generalized gradient approximation level was used^{3,4}. We employed projector augmented wave pseudopotentials^{5,6} as implemented in the Vienna Ab-initio Simulation Package (VASP)⁷. All relaxations were performed with the semi-empirical DFT-D3 van der Waals correction scheme⁸ and with a force threshold of 0.01 eV/Å. Brillouin zone sampling densities were set to be equivalent to $12 \times 12 \times 1$ for a minimal SiC surface unit cell with the in-plane lattice constant $a = 3.19\text{\AA}$. The SiC slab thickness was 6 SiC units, with hydrogen capping included for the other surface (opposite to the Pb-covered surface).

To construct the tight-binding model used in the main text, we adopted a structural approximation – a relaxed minimal SiC surface unit cell with one Pb atom – to perform preparatory self-consistency DFT calculations for Wannier interpolation. These calculations were performed using the Quantum Espresso package⁹ with projector augmented wave pseudopotentials and with k-point grids of $12 \times 12 \times 1$, all other convergence parameters being the same as those used in the VASP calculations. Maximally localized Wannier functions and tight-binding parameters¹⁰ were constructed using the Wannier90 code¹¹. Band disentanglement followed the standard procedure outlined in Ref. [12]: a disentanglement window was chosen to cover the entire energy where bands with all four types of orbital characters (see main text) were present; a frozen window (where Bloch state are forced to be preserved) were chosen to cover a smaller energy range where bands with *exclusively* all four types of orbital characters are present.

C. Numerical Realization

This section discusses the numerical methods based on Ref. [13] to evaluate the formula in Sec. IA.

For the units used in numerical calculation, the length unit is $k_0^{-1} = 1\text{\AA}$ and the energy unit is $\epsilon_0 = 1eV$. The units for other physical quantities are determined from these two units accordingly. For example, the unit for CISP is $\chi_0 = k_0 e\hbar/\epsilon_0$. The unit for $n_i V_0^2$ in Eq. (6) and Eq. (7) is $k_0^2 \epsilon_0^2$. With this unit, the $n_i V_0^2$ is taken to be 0.05 in the main text.

The first BZ integration in Eq. (1), Eq. (2), Eq. (6) and Eq. (7) is replaced by summation over a mesh. The first BZ is a hexagon with three K points located at

$$K = (4\pi/3, 0) \quad K_1 = (4\pi/3 \times \cos 2\pi/3, 4\pi/3 \times \sin 2\pi/3) \quad K_3 = (4\pi/3 \times \cos 4\pi/3, 4\pi/3 \times \sin 4\pi/3) \quad (25)$$

The mesh points are taken to be $k_1 K + k_2 K_1$, $k_1 K_1 + k_2 K_2$ and $k_1 K_2 + k_2 K$, respecting C_3 symmetry to ensure the current conserving (See Sec. ID). The k_1 and k_2 are two real numbers in the range $[0, 1]$ with the mesh step $\Delta k = 0.005 \times 3/4\pi$. The corresponding energy change of adjacent mesh points in spectrum $\Delta\epsilon \sim 0.005$ is roughly an order smaller than the self-energies $\sim n_i V_0^2$. Thus, the BZ integration in Eq. (1), Eq. (2), Eq. (6) and Eq. (7) could be replaced by

$$\int \frac{d^2 \mathbf{k}}{(2\pi)^2} f(\mathbf{k}) \rightarrow \sum_{\mathbf{k}_i} \frac{(\Delta k)^2 \sin 2\pi/3}{(2\pi)^2} f(\mathbf{k}_i) \quad (26)$$

where $\sin(2\pi/3)$ comes from the Jacobin of a parallelogram mesh with the angle $2\pi/3$. In total, there are $n_k \sim 10^6$ points for the mesh.

The self-consistent self-energies and Green's functions in Eq. (3) and Eq. (6) are calculated in an iterative manner. The initial values for self-energies is taken to be $-in_i V_0^2/2$, same as self-energies for 2DEG. After 12 iteration, the difference in self-energies is $\sim 10^{-5} \ll \Delta\epsilon$. Thus, the self-energies are considered as converged to the self-consistent values.

The vertex corrections in Eq. (7) are solved in the following way. We move $\gamma(E)$ out of the matrix multiplication $G^R \gamma G^A$ by rewriting Eq. (7) in the form of the tensor product as

$$\gamma_{j,mn}(E) = \sum_{m',n'} n_i V_0^2 \int \frac{d^2 \mathbf{l}}{(2\pi)^2} (G^R(\mathbf{l}, E) \otimes G^A(\mathbf{l}, E)^T)_{mn,m'n'} (J_{j,m'n'}(\mathbf{l}) + \gamma_{j,m'n'}(E)) \quad (27)$$

where n, m are the basis vector indices, $(G^R \otimes G^A)^T)_{mn,m'n'} = G_{m,m'}^R G_{n',n}^A$ and $J_{j,mn}(\mathbf{l})$ is treated as a vector with the $(m-1) \times n_b + n$ th element as $\langle \mathbf{l}m | J_j | \mathbf{l}n \rangle$. Here n_b is the number of basis. With matrix inversion, we find that the vertex correction is solved as

$$\gamma_j(E) = (1 - n_i V_0^2 \int \frac{d^2 \mathbf{k}}{(2\pi)^2} (G^R(\mathbf{k}, E) \otimes G^A(\mathbf{k}, E)^T))^{-1} n_i V_0^2 \int \frac{d^2 \mathbf{l}}{(2\pi)^2} (G^R(\mathbf{l}, E) \otimes G^A(\mathbf{l}, E)^T) J_j(\mathbf{l}). \quad (28)$$

The dimension of the matrices are of order $\sim O(n_k n_b^2)$. The basis for calculation are the Bloch states transformed from wannier orbitals used in DFT calculation. In these basis, $\gamma_j(E)$ is independent of momenta for short range disorder and only has n_b^2 elements compared to $n_k n_b^2$ elements in energy eigenbasis.

Then we are going to show how to deal with the the integration with the delta function $\delta(E - \epsilon_{kn})$ in Eq. (12), Eq. (23), Eq. (8) and Eq. (14). The delta function $\delta(E - \epsilon_{kn})$ is first integrated out by radial integration as

$$\int \frac{d^2 \mathbf{k}}{(2\pi)^2} \delta(E - \epsilon_{kn}) f(\mathbf{k}) \rightarrow \int \frac{k(\theta) d\theta}{(2\pi)^2} \frac{1}{|\partial \epsilon_{kn} / \partial k|_{k=k(\theta)}} f(k(\theta), \theta). \quad (29)$$

The angular integration is then replaced by a discrete sum as

$$\int \frac{d^2 \mathbf{k}}{(2\pi)^2} \delta(E - \epsilon_{kn}) f(\mathbf{k}) \rightarrow \sum_{\alpha, \theta_i} \frac{k_n^\alpha(\theta_i) \Delta\theta}{(2\pi)^2} \frac{1}{|\partial \epsilon_{kn} / \partial k|_{k=k_n^\alpha(\theta_i)}} f(k_n^\alpha(\theta_i), \theta_i). \quad (30)$$

The $k_i^\alpha(\theta)$ is the interpolated wave vector at the Fermi surface, which is characterized by the parameter θ (the corresponding angle of the momentum) for the α branch of the band n Fermi surface.

Rewrite self-energies in Eq. (8) and vertex correction in Eq. (14) with the interpolated Fermi surfaces as

$$\text{Im} \Sigma^R(k_n^\alpha(\theta_i), E) = n_i V_0^2 \sum_{n', \alpha', \theta'_i} \frac{k_{n'}^{\alpha'}(\theta'_i) \Delta\theta}{(2\pi)^2} \frac{-\pi}{|\partial \epsilon_{kn} / \partial k|_{k=k_{n'}^{\alpha'}(\theta'_i)}} |\langle k_n^\alpha(\theta_i) | k_{n'}^{\alpha'}(\theta'_i) \rangle|^2. \quad (31)$$

$$\gamma_j(k_n^\alpha(\theta_i), E) = n_i V_0^2 \sum_{n', \alpha', \theta'_i} \frac{k_{n'}^{\alpha'}(\theta'_i) \Delta \theta}{(2\pi)^2} \frac{-\pi}{|\partial \epsilon_{kn} / \partial k|_{k=k_{n'}^{\alpha'}(\theta'_i)}} |\langle k_n^\alpha(\theta_i) | k_{n'}^{\alpha'}(\theta'_i) \rangle|^2 \frac{1}{\text{Im} \Sigma^R(k_{n'}^{\alpha'}(\theta'_i), E)} (J_j(k_{n'}^{\alpha'}(\theta'_i)) + \gamma_j(k_{n'}^{\alpha'}(\theta'_i), E)). \quad (32)$$

D. Current conservation

In this section, we focus on solving the vertex correction in Eq. (7) and Eq. (14). We are going to show that the matrix to be inverted for vertex correction has zero determinant and its relation to current conservation.

The zero determinant of the matrix in Eq. (28) to be inverted is illustrated with Eq. (31) and Eq. (32) of Fermi surface contributions. By denoting

$$M_{\mathbf{k}'n'} = M_{k_{n'}^{\alpha'}(\theta'_i)} = \frac{k_{n'}^{\alpha'}(\theta'_i) \Delta \theta}{(2\pi)^2} \frac{-\pi}{|\partial \epsilon_{kn} / \partial k|_{k=k_{n'}^{\alpha'}(\theta'_i)}} \quad (33)$$

$$V_{\mathbf{k}n, \mathbf{k}'n'} = V(k_n^\alpha(\theta_i), k_{n'}^{\alpha'}(\theta'_i)) = n_i V_0^2 |\langle k_n^\alpha(\theta_i) | k_{n'}^{\alpha'}(\theta'_i) \rangle|^2,$$

we have the self energies and the vertex correction as

$$\text{Im} \Sigma^R(\mathbf{k}n, E) = \sum_{\mathbf{k}'n'} V_{\mathbf{k}n, \mathbf{k}'n'} M_{\mathbf{k}'n'} \quad (34)$$

$$\gamma_j(\mathbf{k}n, E) = \sum_{\mathbf{k}'n'} V_{\mathbf{k}n, \mathbf{k}'n'} M_{\mathbf{k}'n'} \frac{1}{\text{Im} \Sigma^R(\mathbf{k}'n', E)} (J_j(\mathbf{k}'n') + \gamma_j(\mathbf{k}'n', E)). \quad (35)$$

The matrix $V_{\mathbf{k}n, \mathbf{k}'n'}$ is symmetric. The matrix to be inverted for the vertex correction is

$$I_{\mathbf{k}n, \mathbf{k}'n'} = \delta_{\mathbf{k}n, \mathbf{k}'n'} - V_{\mathbf{k}n, \mathbf{k}'n'} M_{\mathbf{k}'n'} \frac{1}{\text{Im} \Sigma^R(\mathbf{k}'n', E)}. \quad (36)$$

For the singular value decomposition (SVD) of the matrix I , I has a left eigen vector $e_{L0} = M_{\mathbf{k}n}$ and a right eigen vector $e_{R0} = \text{Im} \Sigma(\mathbf{k}'n', E)$ as shown by

$$\sum_{\mathbf{k}n} M_{\mathbf{k}n} I_{\mathbf{k}n, \mathbf{k}'n'} = M_{\mathbf{k}'n'} - \left(\sum_{\mathbf{k}n} M_{\mathbf{k}n} V_{\mathbf{k}n, \mathbf{k}'n'} \right) M_{\mathbf{k}'n'} \frac{1}{\text{Im} \Sigma^R(\mathbf{k}'n', E)} = 0 \quad (37)$$

$$\sum_{\mathbf{k}'n'} I_{\mathbf{k}n, \mathbf{k}'n'} \text{Im} \Sigma(\mathbf{k}'n', E) = \text{Im} \Sigma(\mathbf{k}n, E) - \sum_{\mathbf{k}'n'} V_{\mathbf{k}n, \mathbf{k}'n'} M_{\mathbf{k}'n'} = 0 \quad (38)$$

with Eq. (34). Both eigenvectors have the eigenvalue 0. As a result, the matrix $I_{\mathbf{k}n, \mathbf{k}'n'}$ has zero determinant.

The existence of a solution to the vertex correction in Eq. (35) implies the current conservation physically. To see that, we re-write the vertex correction in the form of the SVD decomposition of the matrix I as

$$\begin{pmatrix} e_{R0} & e_{R1} & \cdots & e_{Rn} \end{pmatrix} \begin{pmatrix} 0 & & & \\ & \lambda_1 & & \\ & & \ddots & \\ & & & \lambda_n \end{pmatrix} \begin{pmatrix} e_{L0}^\dagger \\ e_{L1}^\dagger \\ \vdots \\ e_{Ln}^\dagger \end{pmatrix} \gamma_j = \tilde{J}_j \quad (39)$$

where e_{Li} e_{Ri} λ_i are other left eigenvectors, right eigenvectors, eigenvalues of I , satisfying $e_{Li}^\dagger e_{Rj} = \delta_{ij}$. The elements of γ_j is $\gamma_j(\mathbf{k}n)$ in Eq. (14) and the elements of \tilde{J}_j is $\sum_{\mathbf{k}'n'} V_{\mathbf{k}n, \mathbf{k}'n'} M_{\mathbf{k}'n'} J_j(\mathbf{k}'n') / \text{Im} \Sigma^R(\mathbf{k}'n', E)$. The condition of the existence of γ_j is

$$e_{L0}^\dagger \tilde{J}_j = \sum_{\mathbf{k}n, \mathbf{k}'n'} M_{\mathbf{k}n} V_{\mathbf{k}n, \mathbf{k}'n'} M_{\mathbf{k}'n'} J_j(\mathbf{k}'n') / \text{Im} \Sigma^R(\mathbf{k}'n', E) = \sum_{\mathbf{k}'n'} M_{\mathbf{k}'n'} J_j(\mathbf{k}'n') = 0. \quad (40)$$

Restoring to the integral form, the condition becomes

$$\int \frac{d^2 \mathbf{k}}{(2\pi)^2} \delta(E - \epsilon_{\mathbf{k}n}) J_j(\mathbf{k}n) = 0. \quad (41)$$

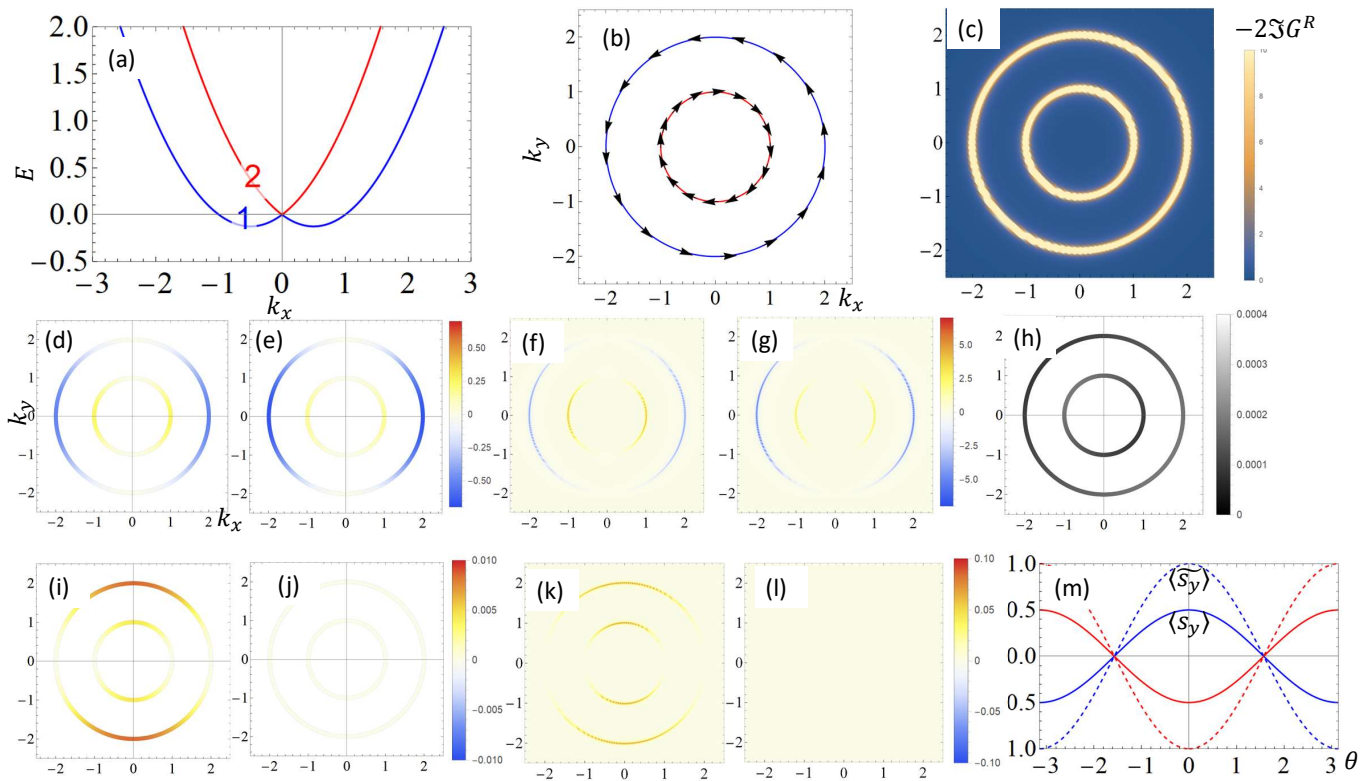


FIG. 1: (a) The spectrum of Rashba 2DEG. (b) The Fermi surface for $E_f = 1$ and the spin texture on the Fermi surface. (c) The spectral weight shown over the Brillouin zone. (d)(e) The contribution to CISP χ_{yx} on the Fermi surface of Eq. (13) without and with vertex correction. (e)(f) The contribution to CISP χ_{xy} over the Brillouin zone of Eq. (4) without and with vertex correction. (h) the relaxation time over the Fermi surfaces $\tau_{kn} + 20$. (i)(j) The contribution to SHE σ_{yx}^z on the Fermi surface of Eq. (24) without and with vertex correction. (k)(l) The contribution to SHE σ_{yx}^z over the Brillouin zone of Eq. (5) without and with vertex correction. (m) The y component of the spin directions on the Fermi surface. The solid (dashed) lines are the spin vertex without (with) the vertex correction. The spin components are shown in the polar angle θ of the Brillouin zone.

Physically, this means the total current of the electrons in equilibrium is zero. Since the charge ρ is conserved, the current conservation $\partial_t \rho + \nabla \cdot \mathbf{J} = 0$ is satisfied.

To solve the vertex correction, the inverse in Eq. (35) shall be replaced by Moore-Penrose pseudo-inverse¹⁴, given by

$$\begin{pmatrix} e_{L0}^\dagger \gamma_j \\ e_{L1}^\dagger \gamma_j \\ \vdots \\ e_{Ln}^\dagger \gamma_j \end{pmatrix} = \begin{pmatrix} 0 & & & \\ & 1/\lambda_1 & & \\ & & \ddots & \\ & & & 1/\lambda_n \end{pmatrix} \begin{pmatrix} e_{L0}^\dagger \tilde{J}_j \\ e_{L1}^\dagger \tilde{J}_j \\ \vdots \\ e_{Ln}^\dagger \tilde{J}_j \end{pmatrix} \quad (42)$$

in the SVD decomposition. Another way to solve for the vertex correction with this non-iterative method is using the finite frequency response $\chi_{ij}(\omega)$ and then decreasing ω for a convergent result in the $\omega \rightarrow 0$ limit.

II. NUMERICAL RESULTS OF SPIN TRANSPORT

A. Rashba 2DEG

To validate our numerical methods, we will first evaluate the spin transport of 2-dimensional electron gas (2DEG) with Rashba spin-orbit coupling, which can be directly compared with the analytical solutions in Ref. [15].

The Hamiltonian of the Rashba 2DEG is

$$H(\mathbf{k}) = k^2/2 + \alpha_R(k_y\sigma_x - k_x\sigma_y). \quad (43)$$

Fig. 1(a) shows the spectrum of two spin splitting bands, with the parameters $\alpha_R = 0.5$ and $E_f = 1$. Fig. 1(b) shows the Fermi surfaces and the spin texture on the Fermi surfaces. The Fermi surfaces are two concentric circles. The spins on the Fermi surfaces of band 1 and 2 are opposite. Fig. 1(c) shows The spectral weight $-2\text{Im}TrG^R(\mathbf{k}, E_f)$ with $n_i V_0^2 = 0.05$. The two bands are clearly resolved in the dilute disorder limit.

We directly compare our numerical results for CISP with theoretical values obtained from Ref. [15] for a typical set of parameters listed above. The CISP from the full numerical calculations of the formula Eq. (1) is -0.79878 without vertex correction and -1.5865 with vertex correction. The simplified formula Eq. (12) only with the Fermi surface contribution gives -0.79572 without vertex corrections and -1.5914 with vertex correction. Thus, the two results from different expressions give nearly identical the CISP response coefficients that also agree with the theoretical values $-\alpha_R/4\pi n_i V_0^2 = -0.79578$ without and $-\alpha_R/2\pi n_i V_0^2 = -1.5916$ with vertex corrections from Ref. [15] within 1%. The error can be reduced by taking denser meshes.

Next we provide an intuitive physical picture for the general understanding of the origin of the CISP χ_{yx} . Under the electrical field along the $+x$ direction, the electrons are in the non-equilibrium states and the corresponding Fermi sphere shifts to the $-x$ direction. For the Fermi surfaces of the band 1 in Fig. 1 (b), less electrons occupy the states with $k_x > 0$ and spin directions $s_y > 0$ while more electrons occupy the states with $k_x < 0$ and spin directions $s_y < 0$. As a result, a charge current in $+x$ direction gives rise to a negative contribution to the CISP χ_{yx} ($s_y < 0$) for the Fermi surface of the band 1, as shown by the blue color in Fig. 1(d)(e)(f)(g). Thus, the electrons on this Fermi surface contributes $\propto (k_f + 2\alpha_R)\tau$. τ is the relaxation time and constant over the whole Fermi surfaces for both bands as shown in Fig. 1(h) with values close to the theoretical one $-n_i V_0^2/2$. The electrons on the Fermi surface of the band 2 gives a positive contribution (red color) to CISP due to the opposite spin texture as shown in Fig. 1(d)(e)(f)(g), which is proportional to $k_f\tau$. Adding the contributions from two Fermi surfaces, we find $\chi_{yx} \propto \alpha_R\tau$.

For the vertex correction, it is more convenient to consider the correction to spin operator instead of current operator. Theoretically, the spin operator with the vertex correction $\langle \mathbf{k}n | \tilde{S}_y(E) | \mathbf{k}n \rangle$ in Eq. (17) doubles the bare spin operator matrix elements $\langle \mathbf{k}n | S_y | \mathbf{k}n \rangle$. Thus, CISP with the vertex correction is $\tilde{\chi}_{yx} = 2\chi_{yx}$. Fig. 1(m) shows the numerical spin operator matrix element from Eq. (17). The spin operator with the vertex correction doubles the bare spin operator over the whole Fermi surfaces, consistent with the theoretical results.

Finally, we show that the numerical results for SHE also agree with theoretical results. The calculated SHE σ_{yx}^z from the formula Eq. (2) are 0.0397802 without vertex correction and 1.26112×10^{-4} with vertex correction. The simplified formula Eq. (23) gives 0.039789 without vertex correction and -2.75749×10^{-4} with vertex corrections. Both agree with each other and are consistent with the theoretical values $1/8\pi$ without vertex correction and 0 with vertex correction from Ref. [16] within the error 1%.

Fig. 1(i)-(l) shows the contribution to the response coefficient σ_{yx}^z of SHE defined by Eq. (24) and Eq. (5). Without vertex correction, the off-diagonal terms contribute a positive value to SHE (red color), which is maximal on the y axis and nearly zero on the x -axis. The diagonal contribution is almost zero as $\langle \mathbf{k}n | J_y^z | \mathbf{k}n \rangle$ is zero. When including the vertex correction, we find the SHE coefficient σ_{yx}^z is almost zero, as predicted by the analytical theory. This reveals the cancellation of the intrinsic and intrinsic-side-jump contributions to SHE¹⁷.

B. Spin texture of monolayer Pb

In this section, we will discuss the physical properties and origins of the momentum-space spin anti-vortex, as well as the relation to the Lifshitz transition of Fermi surfaces.

First, we show the matrix element $\langle \mathbf{k}n | S_i | \mathbf{k}n \rangle$ of spin operator at the location of spin anti-vortex approaches zero. Fig. 2(a) shows the spin direction along the $\Gamma - K$ line. At the high symmetry points Γ and K , the states are degenerate and the spin directions are not well defined. We find the spin directions along this line mainly lies in the plane and point to the y axis as a consequence of the x -directional mirror and time reversal symmetries. As the spin directions near Γ and K are opposite, it has to approach zero at certain momentum in the Γ - K line, which is labelled as k_S in Fig. 2(a).

The spin anti-vortex originates from the anti-crossing between the bands with opposite spin directions. Fig. 2(b) shows the projection of eigen-states to different orbitals, defined as $\langle \mathbf{k}n | P_i | \mathbf{k}n \rangle$ with the projection operator $P_i = |p_i\rangle\langle p_i|$ to the orbital p_i , along $\Gamma - K$. Around k_S , the dominant orbital nature of the bands changes from the p_z orbital of SiC (red line) to the p_x and p_y orbitals of Pb (blue lines). As the orbital nature varies rapidly across the anti-crossing regime, we choose the following condition (the gradient of the probability difference between different

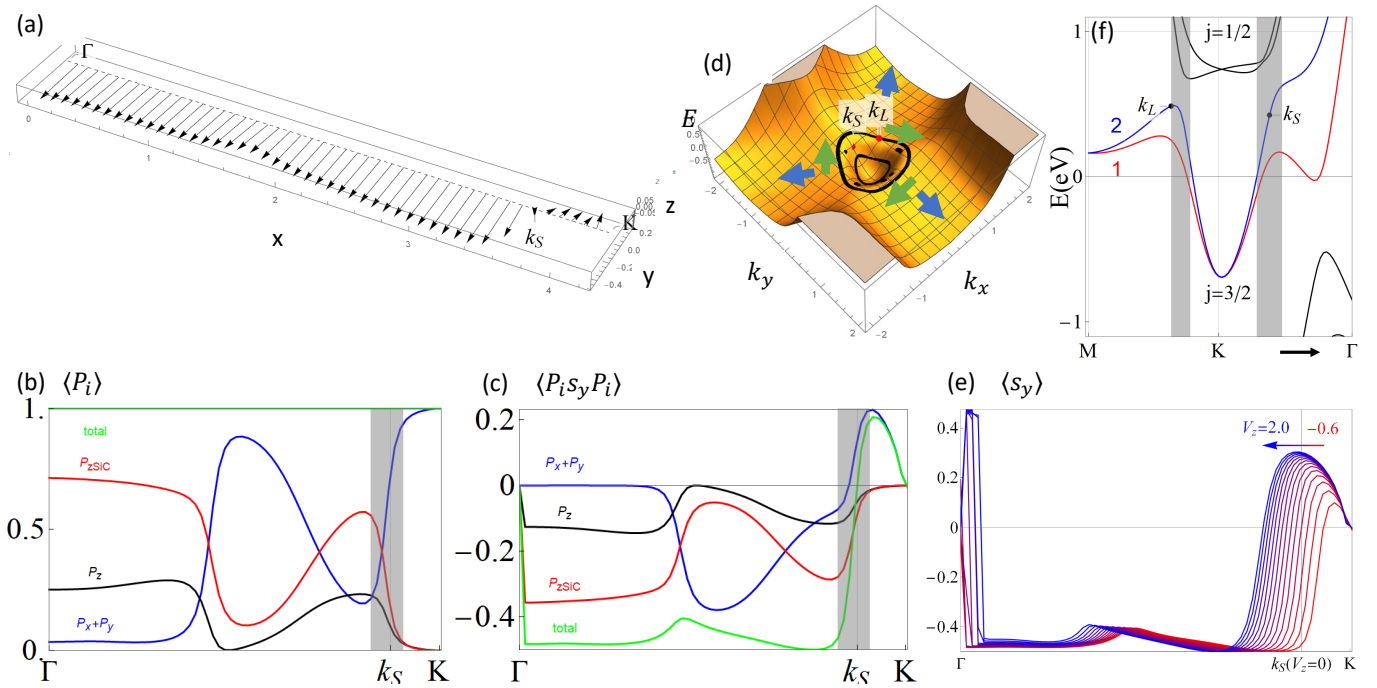


FIG. 2: (a) Spin directions along the $\Gamma - K$ line in 3D. (b) The projection of states along $\Gamma - K$ to different orbitals. The total is the sum of all orbitals. The grey region is the anti crossing region. (c) The contribution to y components of spin directions from different orbitals. (d) The energy spectrum over 2D Brillouin zone around K in 3D. (e) The y components of spin directions from all orbitals for different V_z from -0.6eV to 2.0eV with an interval 0.2eV indicated by the colorful arrow. (f) The energy spectrum with $V_z = 1\text{eV}$.

orbitals)

$$|\nabla_{\mathbf{k}} \langle \mathbf{k}n | P_x + P_y - P_{zSiC} | \mathbf{k}n \rangle| > 1 \quad (44)$$

to determine the anti-crossing regime, as shown by the grey region in Fig. 2(b) and (c). Fig. 2(c) shows the contribution to s_y components from different orbitals $\langle \mathbf{k}n | P_i s_y P_i | \mathbf{k}n \rangle$. The p_{zSiC} orbital carries negative s_y while the p_x and p_y orbitals carry positive s_y . As the orbital nature of the bands varies from the p_{zSiC} orbital to the p_x and p_y orbitals, zero s_y occurs in the anti-crossing regime and determines the location of the spin anti-vortex k_S .

Besides spin anti-vortex, the band anti-crossing also leads to the Lifshitz transition of Fermi surfaces. The Lifshitz transition happens at the saddle points of the spectrum. Fig. 2(d) shows the spectrum around K in the 2D BZ and the saddle point is labeled by k_L . In the anti-crossing region between two black lines, the spectrum shows a loop of local maxima in the radial direction. Along the tangential direction of this loop, the red points are the local minima and these minima define the saddle points in the energy spectrum. The Lifshitz transition happens at these saddle points. In summary, both spin anti-vortex and Lifshitz transition happen in the anti-crossing region as shown in Fig. 2(d).

In addition, the location of the spin anti-vortex can be controlled by an external gate that tunes the difference in potentials between the Pb layer and SiC substrate. To model the effect, we include a constant potential V_z to the p_z orbital of SiC and the energy spectrum for $V_z = 1.0\text{eV}$ is shown in Fig. 2(f). Compared to the Fig. 2(d) in the main text for $V_z = 0\text{eV}$, the $j = 1/2$ bands from the SiC for $V_z = 1\text{eV}$ have higher energies and the band anti-crossing region moves away from K point, which leads to the change of the location of both the Lifshitz transition point k_L and the spin anti-vortex point k_S . To show the movable range of the spin anti-vortex, we plot the y component of spin directions on the $\Gamma - K$ line from all orbitals for different V_z in 2(e). The zeros of these lines around $k_S (V_z = 0)$ indicate the locations of spin anti-vortex points for different V_z . The spin anti-vortex could be moved towards Γ by positive V_z (blue lines) or K by negative V_z (red lines).

C. Numerical CISP for monolayer Pb

In this section, we will focus on understanding the numerical results of CISP for monolayer Pb by comparing with Rashba 2DEG at high E_f and explaining the behaviors of CISP when varying E_f . The numerical calculation by

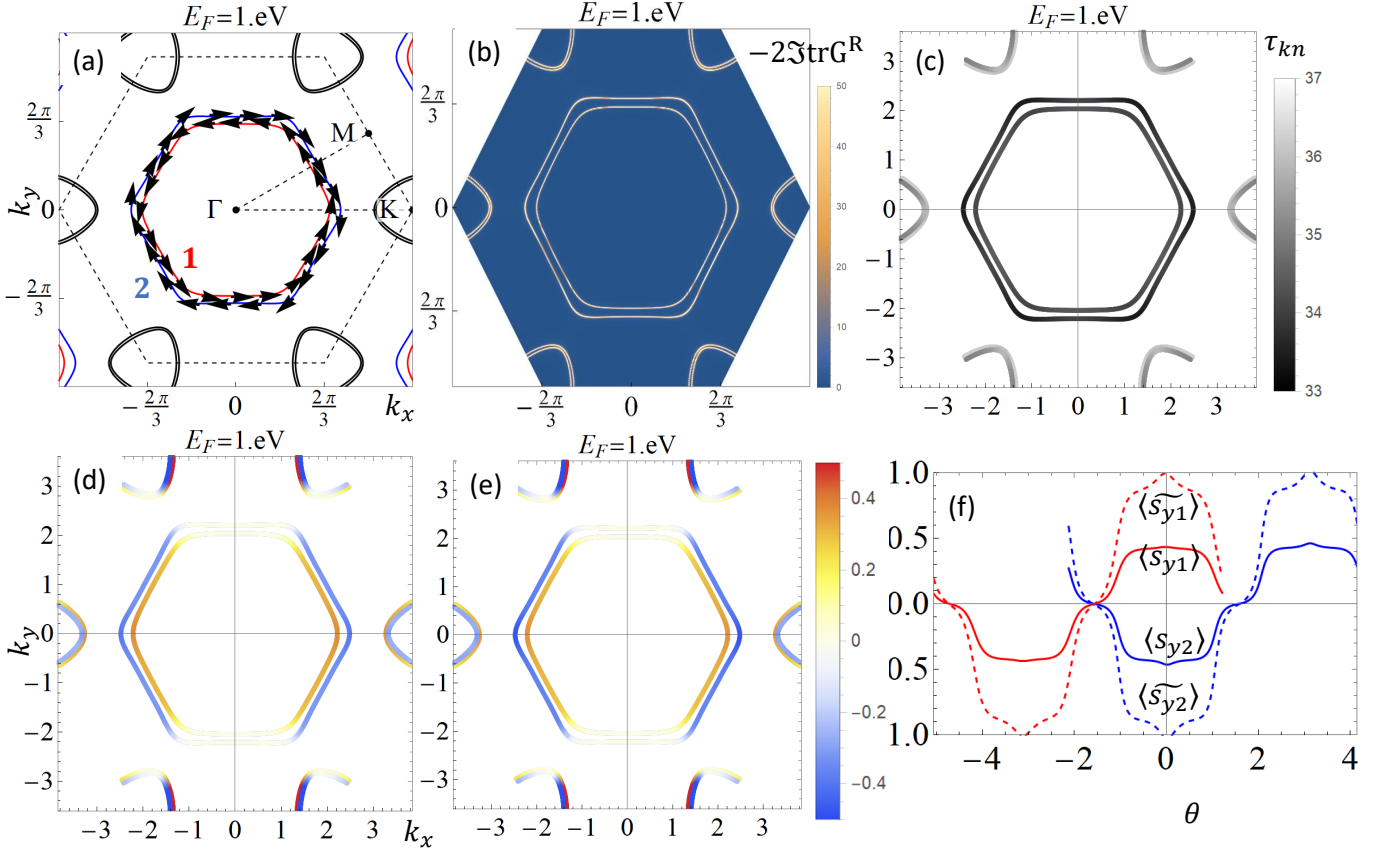


FIG. 3: (a) Fermi surfaces and spin texture for $E_F = 1 \text{ eV}$. (b) Spectral weight for $E_F = 1 \text{ eV}$ over the Brillouin zone. (c) Relaxation time over the Fermi surfaces. (d)(e) The contribution to CISP on Fermi surfaces without and with vertex correction. (f) The s_y over Fermi surfaces for band 1 and 2. The red line (blue) is band 1 (2). The solid line is the bare spin vertex. The dashed line is the corrected spin vertex.

Eq. (12) at $E_F = 1 \text{ eV}$ for the band 1 and 2 in Fig. 3(a) is consistent with the physical picture of Fermi surfaces shift in Rashba 2DEG. To see that, Fig. 3(a) shows the spin texture on the Fermi surfaces of bands 1 and 2, similar to Rashba 2DEG and opposite to each other. All the calculations of CISP are done within dilute disorder limits, for which the band broadening induced by disorder is smaller than spin splitting energies and the spin splitting bands are well resolved in the spectral weight as shown in Fig. 3(b). The corresponding relaxation time is shown in Fig. 3(c), and we find the relaxation time to be uniform for each Fermi surface, but its values for the bands 1 and 2 are slightly different. Another difference from Rashba 2DEG is the Fermi surfaces of band 1 and 2 are hole pockets, not the electron pockets. When electrical fields are applied in the $+x$ direction, rather than less electrons with $k_x > 0$ and $s_y < 0$ for electron pockets, there are more electrons with $k_x > 0$ and $s_y < 0$ and less electrons with $k_x < 0$ and $s_y > 0$. The contribution from this Fermi pocket to CISP is negative (blue color) as shown in Fig. 3(d)(e). The red Fermi surface has the opposite spin texture and contribute positively (red color) as shown in Fig. 3(d)(e). As Rashba 2DEG, the contribution from the blue Fermi pockets is canceled partly by the red one and make a total negative contribution as shown in Fig. 4(a) at $E_f = 1 \text{ eV}$.

Under \mathcal{T} symmetry, the contribution to CISP in Eq. (13) becomes

$$\begin{aligned}
 \chi_{ij}(\mathbf{kn}) &= -\frac{1}{2\pi} \langle \mathbf{kn} | S_i | \mathbf{kn} \rangle \langle \mathbf{kn} | \Gamma_j(\mathbf{k}, E_f) | \mathbf{kn} \rangle \delta(E_f - \epsilon_{\mathbf{kn}}) \frac{\pi}{-\text{Im} \Sigma^R(\mathbf{kn}, E_f)} \\
 &= -\frac{1}{2\pi} \langle -\mathbf{kn} | (\mathcal{T} S_i \mathcal{T}^\dagger) | -\mathbf{kn} \rangle^* \langle -\mathbf{kn} | (\mathcal{T} \Gamma_j(\mathbf{k}, E_f) \mathcal{T}^\dagger) | -\mathbf{kn} \rangle^* \delta(E_f - \epsilon_{\mathbf{kn}}) \frac{\pi}{-\text{Im} \Sigma^R(\mathbf{kn}, E_f)} \\
 &= -\frac{1}{2\pi} \langle -\mathbf{kn} | (-S_i) | -\mathbf{kn} \rangle^* \langle -\mathbf{kn} | (-\Gamma_j(\mathbf{k}, E_f)) | -\mathbf{kn} \rangle^* \delta(E_f - \epsilon_{-\mathbf{kn}}) \frac{\pi}{-\text{Im} \Sigma^R(-\mathbf{kn}, E_f)} \\
 &= \chi_{ij}(-\mathbf{kn}).
 \end{aligned} \tag{45}$$

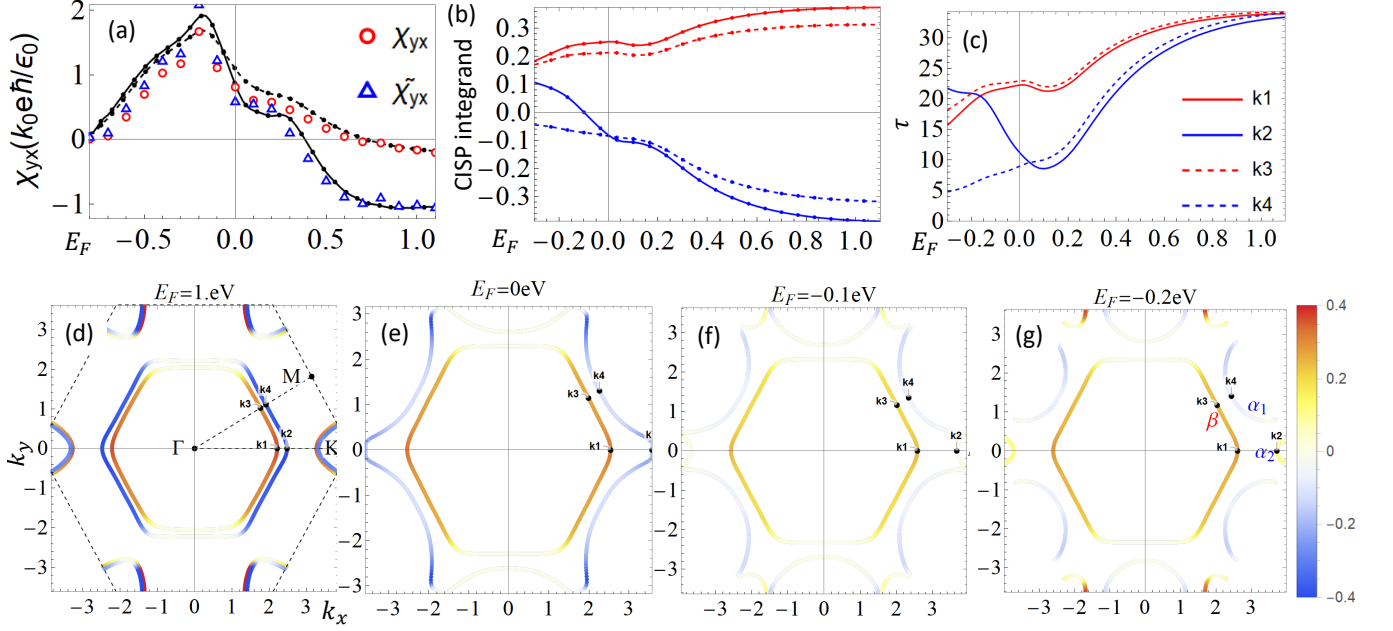


FIG. 4: (a) CISP. The solid (dashed) line is calculated from the Brillouin zone formula Eq. (1) with (without) vertex correction. The red circles (blue triangles) are calculated from the Fermi surface formula Eq. (12). (b)(c) The contribution to CISP and relaxation time at the intersection points $k_1 k_2 k_3 k_4$ between the Fermi surfaces of band 1 and 2 and the high symmetry lines $\Gamma-K$ and $\Gamma-M$ lines. (d)(e)(f)(g) the contribution to CISP over the Fermi surfaces Eq. (13) for $E_F = 1eV, 0eV, -0.1eV, -0.2eV$.

This means the contribution to CISP should be the same at \mathbf{k} and $-\mathbf{k}$, which is clearly shown by the numerical calculations in Fig. 3(d)(e) and Fig. 4(d)-(g).

We also find that the vertex correction increases the matrix elements of the spin operator, similar to the case of Rashba 2DEG. Fig. 3(f) shows the corrected spin operator in Eq. (17) is proportional to and larger than the bare spin operator and share similar profiles over θ .

The numerical calculations of the CISP from Eq. (12) and Eq. (1) are shown by solid (dashed) lines and circles (triangles) in Fig. 4(a) for the cases with (without) vertex corrections for different E_F . Interestingly, we notice a sign change of the CISP when lowering E_F from 1eV to 0eV and a rapid change around $E_F = -0.1eV$. The sign change originates from the different relaxation time for the bands 1 and 2. Fig. 4(c) shows the relaxation time on four typical points k_1 to k_4 for different E_F . The four points are intersection points between Fermi surfaces of band 1 and 2 with the high symmetry lines $\Gamma-K$ and $\Gamma-M$. Fig. 4(b) shows the contribution to CISP at these points. Around $E_F = 1eV$, the relaxation time for all the momenta in Fig. 4(c) has a similar magnitude, which indicates a similar relaxation time for the bands 1 and 2. Correspondingly, the sign of the CISP is determined by the Fermi surface size of the bands 1 and 2, and since the band 2 has a large Fermi surface size, the CISP coefficient χ_{yx} has a negative sign. When lowering E_F to 0eV, the relaxation time of the band 2 (blue lines) decreases more rapidly than that of the band 1 (red lines) in Fig. 4(c), which leads to a dominant contribution from the band 1 for the CISP and thus, χ_{yx} changes its sign to be positive around $E_F = 0eV$.

Besides the sign change, we also notice a rapid change in CISP coefficient χ_{yx} between $E_F = 0eV$ and $E_F = -0.2eV$, which is closely related to the spin anti-vortex around $E_F = -0.1eV$. When lowering $E_F = 0eV$ to $E_F = -0.2eV$, the Fermi pocket α_2 around the K point comes across spin anti-vortex at k_S . The spin texture at two sides of the spin anti-vortex are opposite along the $\Gamma-K$ line as shown in Fig. 2(a). Furthermore, the α_2 Fermi pockets in Fig. 4(g) have a relatively large relaxation time. This means the contribution of CISP from the Fermi pockets α_2 of the band 2 has the same sign as that from the band 1, thus leading to a rapid increasing of the CISP around $E_F = -0.1eV$ in Fig. 4(a).

The rapid change in CISP shows a special feature of spin anti-vortex that it is located at non-high-symmetry momenta when compared to the spin vortex texture located at time reversal invariant momenta in the Rashba model. This is explained as follows. First, we can consider a time reversal invariant momentum. Such a momentum is always enclosed by a Fermi pocket since opposite momenta around a time reversal invariant momentum have to be both occupied or unoccupied; e.g. Γ is always enclosed by the Fermi surface β independent of E_F , unless the whole Fermi surface completely disappears. Next, we consider a spin anti-vortex that is located at a non-high-symmetry

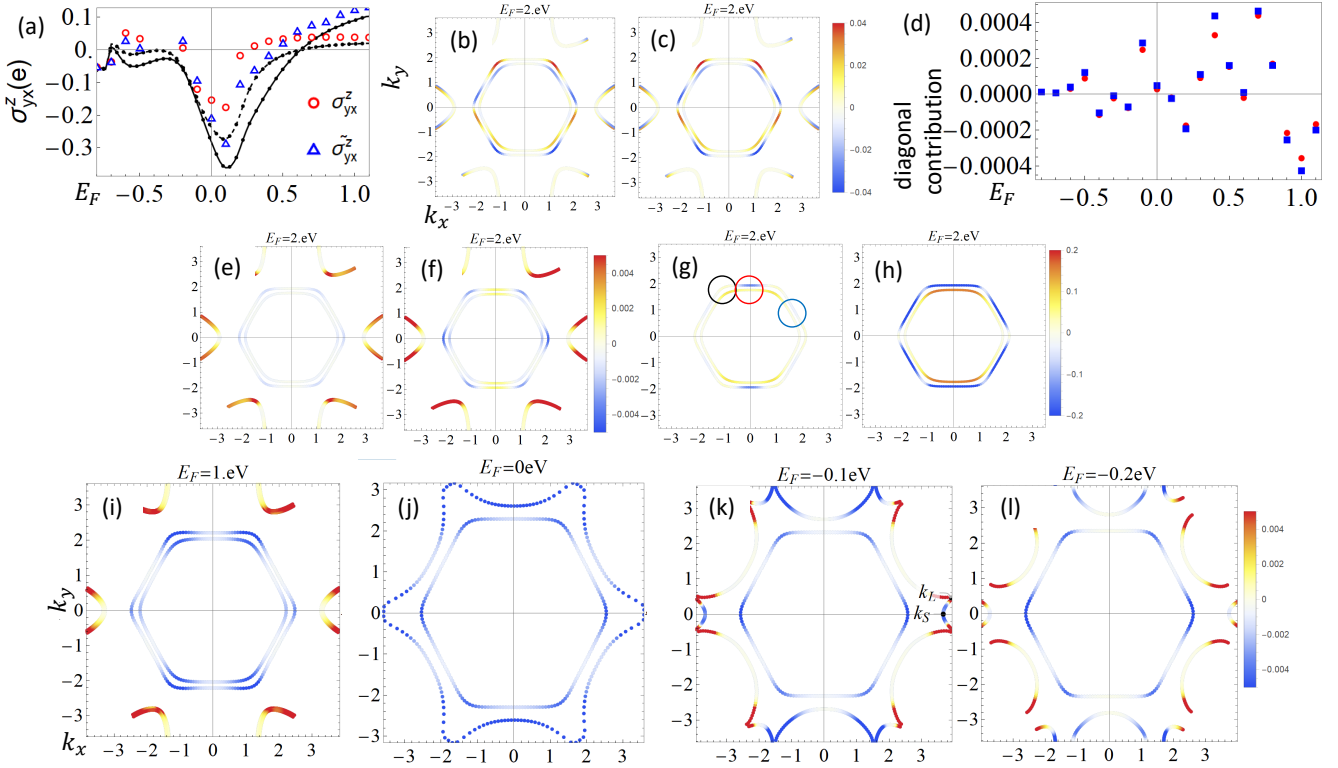


FIG. 5: (a) SHE. The solid (dashed) line is calculated from the Brillouin zone formula Eq. (2) with (without) vertex correction. The red circles (blue triangles) are calculated from the Fermi surface formula Eq. (23). (b)(c) The diagonal contribution to SHE over Fermi surfaces at $E_F = 2eV$ without and with vertex corrections. (d) The diagonal contribution to SHE for different E_F . (e)(f) The off diagonal contribution to SHE over Fermi surfaces at $E_F = 2eV$ without and with vertex corrections. (g) $\text{Im}(\langle \mathbf{k}n' | J_i^k | \mathbf{k}n \rangle \langle \mathbf{k}n | J_j(\mathbf{k}, E_f) | \mathbf{k}n' \rangle)$ over Fermi surfaces of $E_F = 2eV$. (h) $\text{Im}(\langle \mathbf{k}n' | J_i^k | \mathbf{k}n \rangle \langle \mathbf{k}n | \Gamma_j(\mathbf{k}, E_f) | \mathbf{k}n' \rangle)$ including vertex corrections. (i)(j)(k)(l) the off diagonal contribution to SHE over the Fermi surfaces for $E_F = 1eV, 0eV, -0.1eV, -0.2eV$ with vertex corrections.

momentum. Consequently, it allows the Fermi surface to pass through the anti-vortex core as E_F varies: e.g. as E_F lowers in Fig. 4(e), the Fermi surface α (red) passes through k_S and evolves into the Fermi surface α_2 (green). The Fermi surfaces before and after passing through the spin anti-vortex core have opposite spin textures and thus the contribution from the spin anti-vortex to the CISP can change its sign rapidly. Fig. 4(e) and (g), where E_F is lowered and the CISP contribution from the Fermi surface near k_S changes from negative (blue, from the Fermi surface α) to positive (red, from the Fermi surface α_2). In comparison, the spin polarization at the Fermi pocket β around Γ in Fig. 4(e) and (g) keeps the positive sign (red) and can only vary relatively slowly.

D. Numerical SHE for monolayer Pb

In this section, we discuss the numerical calculations of the SHE coefficient of monolayer Pb shown in Fig. 5(a). For σ_{yx}^z at high E_F , we check our calculation and compare with Rashba 2DEG. When lowering E_F from $1eV$ to $0eV$, there is a sign change of σ_{yx}^z and for E_F between $0.1eV$ and $-0.2eV$, σ_{yx}^z are changing rapidly, which are explained next.

To validate our results, we first examine \mathcal{T} symmetry property of the numerical results. Fig. 5(b) and (c) show the diagonal contribution to the SHE (Eq. (20)) at Fermi surfaces, which is opposite at \mathbf{k} and $-\mathbf{k}$, as required by \mathcal{T} . When summed over Fermi surfaces, the diagonal contribution shown in Fig. 5(d) is negligible as Eq. (20) expected. It can be made closer to zero by taking more points on Fermi surfaces. For off-diagonal contribution ($n' \neq n$ in the

equation below), \mathcal{T} symmetry gives

$$\begin{aligned}
\sigma_{ij}^k(\mathbf{k}n) &= -\frac{1}{2\pi} \sum_{n' \neq n} 2\pi\delta(E_f - \epsilon_{\mathbf{k}n}) \frac{1}{\epsilon_{\mathbf{k}n} - \epsilon_{\mathbf{k}n'}} \text{Im}(\langle -\mathbf{k}n' | (\mathcal{T} J_i^k \mathcal{T}^\dagger) | -\mathbf{k}n \rangle^* \langle -\mathbf{k}n | (\mathcal{T} \Gamma_j(\mathbf{k}, E_f) \mathcal{T}^\dagger) | -\mathbf{k}n' \rangle^*). \\
&= -\frac{1}{2\pi} \sum_{n' \neq n} 2\pi\delta(E_f - \epsilon_{\mathbf{k}n}) \frac{1}{\epsilon_{\mathbf{k}n} - \epsilon_{\mathbf{k}n'}} (-) \text{Im}(\langle -\mathbf{k}n' | (J_i^k) | -\mathbf{k}n \rangle \langle -\mathbf{k}n | (-\Gamma_j(\mathbf{k}, E_f)) | -\mathbf{k}n' \rangle) \\
&= -\frac{1}{2\pi} \sum_{n' \neq n} 2\pi\delta(E_f - \epsilon_{-\mathbf{k}n}) \frac{1}{\epsilon_{-\mathbf{k}n} - \epsilon_{-\mathbf{k}n'}} (-) \text{Im}(\langle -\mathbf{k}n' | (J_i^k) | -\mathbf{k}n \rangle \langle -\mathbf{k}n | (-\Gamma_j(\mathbf{k}, E_f)) | -\mathbf{k}n' \rangle) \\
&= \sigma_{ij}^k(-\mathbf{k}n).
\end{aligned} \tag{46}$$

So the off diagonal contribution should share the same color at opposite momenta, consistent with the calculated one shown in Fig. 5(e)(f).

The cancellations between intrinsic and intrinsic-side-jump contribution in Rashba 2DEG¹⁷ does not happen for monolayer Pb because the band 1 and 2 at large E_F is quantitatively different from the Rashba model. Fig. 5(g) and (h) show $\text{Im}(\langle \mathbf{k}n' | J_i^k | \mathbf{k}n \rangle \langle \mathbf{k}n | \Gamma_j(\mathbf{k}, E_f) | \mathbf{k}n' \rangle)$ in Eq. (23) without and with vertex correction. In contrast, for Rashba 2DEG, it is known that

$$\text{Im}(\langle \mathbf{k}n' | J_i^k | \mathbf{k}n \rangle \langle \mathbf{k}n | J_j(\mathbf{k}, E_f) | \mathbf{k}n' \rangle) = \frac{vk_y^2}{2k} \tag{47}$$

without vertex corrections and 0 including vertex corrections. Thus, it is clear that this quantity $\text{Im}(\langle \mathbf{k}n' | J_i^k | \mathbf{k}n \rangle \langle \mathbf{k}n | \Gamma_j(\mathbf{k}, E_f) | \mathbf{k}n' \rangle)$ shows different behaviors for monolayer Pb and Rashba model.

We next consider the sign change in Fig. 5(a). It can be understood from the disappearance of the two electron Fermi pockets with positive contribution (red color) in Fig. 5(i). At $E_F = 1eV$, the electron Fermi pockets dominate, giving positive contribution. At $E_F = 0eV$, the electron Fermi pockets disappear and the hole Fermi pockets of band 1 and 2 gives negative contribution. So when lowering E_F from $1eV$ to $0eV$, there is a sign change of σ_{yx}^z .

The rapid change is related to the Lifshitz transition of Fermi surfaces of band 2 happened at k_L around $E_F = -0.1eV$. At $E_F = -0.1eV$, the contribution on Fermi surfaces around k_L switches from negative (blue) to positive (red) values as shown in Fig. 5(j)(k)(l). The contribution remains negative around spin anti-vortex. Because contribution around k_L change its sign in a narrow energy range, the total contribution has a large variation.

E. Estimate of the experimental observables

In this section, we will give a numerical estimate of the magnitude of χ_{yx} and σ_{yx}^z and compare the values with those estimated from Rashba 2DEG. In the estimate below, we choose the parameter combination $n_i V_0^2 = 0.05eV^2 \text{\AA}^{-2}$ to characterize the impurity density and strength.

To compare with Rashba 2DEG, the mobility μ is extracted from the longitudinal conductivity $\sigma_{xx} = ne\mu$. $n = \sum_{n\mathbf{k}} \theta(E_F - \epsilon_{\mathbf{k}n})$ is the carrier density. The effective mass is evaluated from the density of states $D = m/\pi\hbar^2$ and the Rashba SOC strength is evaluated from spin splitting energy $\Delta\epsilon/2k_F$ averaged over Fermi surfaces of band 1 and 2. $\Delta\epsilon = \epsilon_{k_F,4} - \epsilon_{k_F,3}$ and k_F is combined with m for the averaged Fermi velocity $v_F = k_F/m$.

The comparisons between monolayer Pb and Rashbs 2DEG are shown in Fig. 6 and they share same order of magnitude. The mobility is fitted to be $\sim 50\text{cm}^2/Vs$ from σ_{xx} . Other response quantities for Rashba 2DEG are calculated in the following way

$$\chi_{yx} = -\frac{1}{2\pi} \tau \alpha_R \frac{me}{\hbar} = -\frac{1}{4} D \mu \frac{\Delta\epsilon}{v_F} \tag{48}$$

$$\sigma_{yx}^z = \frac{e}{8\pi} \tag{49}$$

The spin hall angle is

$$\frac{e \sigma_{yx}^z}{\hbar \sigma_{xx}} = \frac{e}{\hbar} \frac{1}{8\pi n \mu} \tag{50}$$

* Electronic address: cxl56@psu.edu

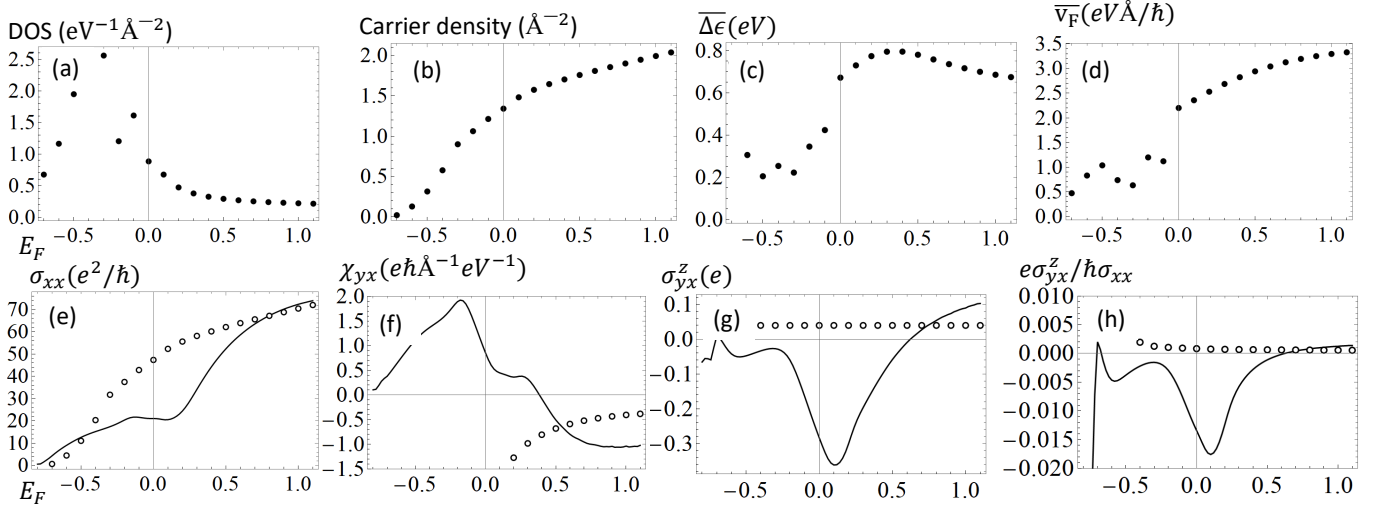


FIG. 6: (a)(b)(c)(d) Density of states, carrier density, average of spin splitting energy, average of Fermi velocity with band 1 and 2 for different E_F (e)(f)(g)(h) comparison between numerical results of monolayer Pb and Rashba 2DEG in longitudinal conductivity, CISP, SHE, spin hall angle over E_F . The solid line is the numerical response functions with vertex corrections. The black circles are calculated with the Rashba 2DEG model.

- ¹ G. D. Mahan, *Many-particle physics* (Springer Science & Business Media, 2013).
- ² N. Briggs, B. Bersch, Y. Wang, J. Jiang, R. J. Koch, N. Nayir, K. Wang, M. Kolmer, W. Ko, A. D. L. F. Duran, *et al.*, *Nature materials* **19**, 637 (2020).
- ³ J. P. Perdew, K. Burke, and M. Ernzerhof, *Phys. Rev. Lett.* **77**, 3865 (1996).
- ⁴ J. P. Perdew, K. Burke, and M. Ernzerhof, *Phys. Rev. Lett.* **78**, 1396 (1997).
- ⁵ P. E. Blöchl, *Phys. Rev. B* **50**, 17953 (1994).
- ⁶ G. Kresse and D. Joubert, *Phys. Rev. B* **59**, 1758 (1999), arXiv:0927-0256(96)00008 [10.1016] .
- ⁷ G. Kresse and J. Furthmüller, *Phys. Rev. B* **54**, 11169 (1996).
- ⁸ S. Grimme, J. Antony, S. Ehrlich, and H. Krieg, *J. Chem. Phys.* **132**, 154104 (2010).
- ⁹ P. Giannozzi, S. Baroni, N. Bonini, M. Calandra, R. Car, C. Cavazzoni, D. Ceresoli, G. L. Chiarotti, M. Cococcioni, I. Dabo, A. D. Corso, S. Fabris, G. Fratesi, S. de Gironcoli, R. Gebauer, U. Gerstmann, C. Gougoussis, A. Kokalj, M. Lazzeri, L. Martin-Samos, N. Marzari, F. Mauri, R. Mazzarello, S. Paolini, A. Pasquarello, L. Paulatto, C. Sbraccia, S. Scandolo, G. Sclauzero, A. P. Seitsonen, A. Smogunov, P. Umari, and R. M. Wentzcovitch, *J. Phys. Condens. Matter* **21**, 395502 (2009), arXiv:0906.2569 .
- ¹⁰ N. Marzari and D. Vanderbilt, *Phys. Rev. B* **56**, 12847 (1997).
- ¹¹ A. A. Mostofi, J. R. Yates, Y.-S. Lee, I. Souza, D. Vanderbilt, and N. Marzari, *Comput. Phys. Commun.* **178**, 685 (2008).
- ¹² I. Souza, N. Marzari, and D. Vanderbilt, *Phys. Rev. B* **65**, 035109 (2001).
- ¹³ Y.-W. Wei, C.-K. Li, Y. Cao, and J. Feng, *Computer Physics Communications* **258**, 107551 (2021).
- ¹⁴ J. C. A. Barata and M. S. Hussein, *Brazilian Journal of Physics* **42**, 146 (2012).
- ¹⁵ J.-i. Inoue, G. E. Bauer, and L. W. Molenkamp, *Physical Review B* **67**, 033104 (2003).
- ¹⁶ J.-i. Inoue, G. E. Bauer, and L. W. Molenkamp, *Physical Review B* **70**, 041303 (2004).
- ¹⁷ J. Sinova, S. O. Valenzuela, J. Wunderlich, C. Back, and T. Jungwirth, *Reviews of Modern Physics* **87**, 1213 (2015).